Investigating the role of dust in ice nucleation within clouds and further effects on the regional weather system over East Asia

Part I: model development and validation

Lin Su[1], and Jimmy C.H. Fung[2, 3]

[1] School of Science, Hong Kong University of Science and Technology, Hong Kong, China

[2] Division of Environment, Hong Kong University of Science and Technology, Hong Kong, China

[3] Department of Mathematics, Hong Kong University of Science and Technology, Hong Kong, China

Correspondence to: Lin Su (lsu@connect.ust.hk)

Highlights:

A new treatment has been implemented in a regional model for evaluating the role of dust particles in atmospheric ice nucleation.

The effect of dust on atmospheric IWC over East Asia during a dust-intensive period is simulated.

The simulation of atmospheric IWC during dust events is substantially improved upon the effect of dust being considered.

Abstract. The GOCART–Thompson microphysics scheme coupling the GOCART aerosol model and the aerosol-aware Thompson-Eidhammer microphysics scheme has been implemented in the WRF-Chem, to quantify and evaluate the effect of dust on the ice nucleation process in the atmosphere by serving as ice nuclei. The performance of the GOCART-Thompson microphysics scheme in simulating the effect of dust in atmospheric ice nucleation is then evaluated over East Asia during spring, a typical dust-intensive season, in 2012. Based upon the dust emission reasonably reproduced by WRF-Chem, the effect of dust on atmospheric cloud ice water content is well reproduced. With abundant dust particles serving as IN, the simulated ice water mixing ratio and ice crystal number concentration increases by 15% and 7% in average over the dust source region and downwind areas during the investigated period. The comparison with ice water path from satellite observations demonstrated that the simulation of cloud ice profile is substantially improved by considering the indirect effect of dust particles in the simulations. Additional sensitivity experiments are carried out to optimize the parameters in the ice nucleation parameterization in the GOCART–Thompson microphysics scheme. Results suggest that lowering the threshold relative humidity with respect to ice to 100% for the ice nucleation parameterization leads to further improvement in cloud ice simulation.

1 Introduction

Dust aerosol is the second largest contributor to the global aerosol burden (Textor et al., 2006), and it is estimated to contribute around 20% to the annual global aerosol emission (Tomasi et al., 2017). The Intergovernmental Panel on Climate Change (IPCC) has recognized dust as a major component of atmospheric aerosols, which are an "essential climate variable." East Asia is a main contributor to the Earth's dust emission. It has been reported in previous studies that East Asian dust contributes 25–50% of global emission, depending on the climate of the particular year (Ginoux et al., 2001).

Dust in the atmosphere alters the Earth's weather and climate through certain ways. By reflecting, absorbing and scattering the incoming solar radiation, dust can cause a warming effect within the atmosphere and a cooling effect at the surface layer (Lacis, 1995), which is the direct effect of dust. The semi-direct effect of dust is related to the absorption of short-wave and long-wave radiation by dust aerosol within clouds, leading to a warming of the surrounding environment, causing a shrinking of cloud and a lower cloud albedo, and thus modifying the radiation budget (Perlwitz and Miller, 2010;Hansen et al., 1997). The dust-cloud-interaction is also referred to as the indirect effect of dust. Dust particles are recognized as effective IN and play an important role in the ice nucleation process in the atmosphere, directly affecting the dynamics in ice and mixed-phase clouds, such as the formation and development of clouds and precipitation (Koehler et al., 2010;Twohy et al., 2009).

To date, many studies have been conducted to evaluate the direct radiative effect of dust aerosol using radiation schemes implemented in numerical models all over the world (Mallet et al., 2009;Nabat et al., 2015a;Ge et al., 2010;Hartmann et al., 2013;Huang et al., 2009;Bi et al., 2013;Liu et al., 2011a;Liu et al., 2011b;Huang, 2017). Recently, semi-direct effect of dust has been investigated in a few studies over different regions by applying various global and regional models (Tesfaye et al., 2015;Nabat et al., 2015b;Seigel et al., 2013). Unfortunately, due to the poor understanding on the dust-cloud-interactions in microphysics processes, quantifying the microphysical effect of dust remains as a difficult problem. Various ice nucleation parameterizations have been implemented into global models to estimate the importance of dust in atmospheric ice nucleation (Lohmann and Diehl, 2006;Karydis et al., 2011;Hoose et al., 2008;Zhang et al., 2014). However, most regional models are not capable of estimating the indirect effect of dust, and vary rare work has been done to assess the indirect effects of dust on the weather system, especially over East Asia, which is a major contributor to the global dust emission. Currently, only a few microphysics schemes

3

61   considering aerosol-cloud-interaction are implemented in regional models. In most of these microphysics schemes

62   only the cloud condensation nuclei (CCN) served by aerosols are considered (Perlwitz and Miller, 2010;Solomos et

63   al., 2011;Miller et al., 2004), while IN are not treated or represented by a prescribed IN distribution (Chapman et al.,

64   2009;Baró et al., 2015), and the production of ice crystals is simplified by a function of temperature or ice saturation.

65   In reality, however, the number of ice crystals that can form in the atmosphere is highly dependent on the number of

66   particles that can act as IN, and dust is the most abundant aerosol that can effectively serve as IN and affect the

67   formation and development of mixed-phase and ice clouds in the atmosphere. This effect should not be neglected in

68   numerical models, especially in the simulations over arid regions during strong wind events (DeMott et al.,

69   2003;Koehler et al., 2010;DeMott et al., 2015;Lohmann and Diehl, 2006;Atkinson et al., 2013).

70   In 2014, the aerosol-aware Thompson-Eidhammer microphysics scheme, which takes into account the aerosols

71   serving as CCN and IN, has been implemented into the Weather Research and Forecast (WRF) model and also the

72   Weather Research and Forecast model coupled with Chemistry (WRF-Chem), enabling the model to explicitly predict

73   the number concentration for cloud droplets and ice crystals (Thompson and Eidhammer, 2014). Therefore, the

74   aerosol-aware Thompson-Eidhammer scheme is an ideal microphysics scheme for evaluating the effect of dust in

75   atmospheric ice nucleation processes. However, this scheme is not coupled with any aerosol model in WRF-Chem,

76   the Weather Research and Forecast model coupled with Chemistry. When the aerosol-aware Thompson-Eidhammer

77   microphysics scheme is activated, the model reads in pre-given climatological aerosol data derived from the output of

78   other global climate models, which introduces large errors into the estimation of the effects of dust in microphysical

79   processes. This problem can be solved by embedding a dust scheme into Thompson-Eidhammer scheme, or by

80   coupling the microphysics scheme with WRF-Chem. Compared with WRF, WRF-Chem integrates various emission

81   schemes and aerosol mechanisms for simulating the emission, transport, mixing, and chemical transformation of

82   aerosols simultaneously with the meteorology (Grell et al., 2013). Therefore, WRF-Chem is more capable of

83   producing a realistic aerosol field by comparing the performances of different emission schemes or aerosol

84   mechanisms.

85   In light of above, we aim to fully couple the aerosol-aware Thompson-Eidhammer microphysics scheme with the

86   Goddard Chemistry Aerosol Radiation and Transport (GOCART) model (Ginoux et al., 2001) in the WRF-Chem

87   modeling system in this study, enabling WRF-Chem to simultaneously simulate the effect of dust aerosol in ice

88   nucleation processes during simulations. Based upon the implementation, the performance of the coupled GOCART-

89   Thompson microphysics scheme in simulating the ice nucleation process involving dust particles was validated and

90   the role that East Asian dust plays in the ice nucleation process in the atmosphere was further investigated.

91   The remainder of the manuscript is presented as follows. Section 2 provides a description of the model including, and

92   the implementation work for coupling the aerosol-aware Thompson-Eidhammer microphysics scheme and the

93   GOCART aerosol model in WRF-Chem is elaborated in Section 3, followed by the model configurations for numerical

94   simulations in section 4. Section 5 presents the observational data used to validate the performance of the GOCART-

95   Thompson microphysics scheme. Section 6 is the results and discussion, followed by the conclusions in section 7.

96

2 Model description

98   WRF-Chem is an online-coupled regional modeling system, which means that it can simultaneously simulate the

99   meteorological field, the chemical field, and the interactions in between (Grell et al., 2013). The chemical model

100   contains several gas- and aerosol-phase chemical schemes. In this study, we focus on the GOCART model, a simple

101   aerosol model that will be used for dust simulation.

102

2.1 GOCART aerosol model

104   GOCART is an aerosol model for simulating major tropospheric natural-source aerosol components, such as sulfate,

105   mineral dust, black carbon, organic carbon, and sea-salt aerosols (Ginoux et al., 2001;Chin et al., 2000). It has been

106   implemented into WRF-Chem as a bulk aerosol scheme. GOCART is a simple aerosol scheme that can predict the

107   mass of aerosol components, but does not account for complex chemical reactions. Therefore, it is numerically

108   efficient in simulating aerosol transport, and thus applicable to cases without many chemical processes, especially

109   dust events. Typically it requires 40% to 50% more computational time by applying WRF-Chem run with GOCART

110   aerosol model than the standard WRF to produce the same period of simulation.

111   Shao's dust emission scheme (Kang et al., 2011;Shao, 2004, 2001;Shao et al., 2011) is one of the dust emission

112   schemes in the GOCART aerosol model, and has been demonstrated to exhibit superior performance in reproducing

113 the dust cycle over East Asia compared to other emission schemes (Su and Fung, 2015). The Shao's emission scheme

114 was updated in WRF-Chem since version 3.8 released in 2016 to produce five size bins for dust emission, with

115 diameters of < 2 μm, 2–3.6 μm, 3.6–6.0 μm, 6.0–12.0 μm, and 12.0–20.0 μm, and mean effective radii of 0.73 μm,

116 1.4 μm, 2.4 μm, 4.5 μm, and 8.0 μm.

117

2.2 Thompson-Eidhammer microphysics scheme

119 The Thompson microphysics scheme is a bulk two-moment aerosol-aware microphysics scheme that considers the

120 mixing ratios and number concentrations for five water species: cloud water, cloud ice, rain, snow and a hybrid

121 graupel/hail category (Thompson et al., 2004). The updated Thompson-Eidhammer scheme is an aerosol-aware

122 version of the Thompson scheme (Thompson and Eidhammer, 2014), which incorporates the activation of aerosols

123 serving as cloud condensation nuclei and IN, and therefore it explicitly predicts the number concentrations of CCN

124 and IN, as well as the number concentrations of cloud droplets and ice crystals. Hygroscopic aerosols that serve as

125 cloud condensation nuclei are referred to as water-friendly aerosols, and those non-hygroscopic ice-nucleating

126 aerosols are referred to as ice-friendly aerosols. The cloud droplets nucleate from explicit aerosol number

127 concentrations using a look-up table for the activated fraction as determined by the predicted temperature, vertical

128 velocity, number of available aerosols, and pre-determined values of the hygroscopicity parameter and aerosol mean

129 radius.

130 In the Thompson-Eidhammer scheme, the ice nucleation process is triggered once the relative humidity with respect

131 to ice (RH_i) exceeds 105%. Furthermore, when the relative humidity with respect to water (RH_w) is above 98.5%, it

132 is counted as condensation and immersion freezing, and calculated by DeMott's parameterization scheme (DeMott et

133 al., 2010); when RH_w is below 98.5%, it is treated as deposition nucleation, and determined by the Phillips'

134 parameterization scheme (Phillips et al., 2008). Both DeMott's scheme and Phillips' scheme are coupled with

135 concentration of ice-friendly aerosols. In addition, the freezing of deliquesced aerosols using the hygroscopic aerosol

136 concentration is parameterized following Koop's parameterization scheme (Koop et al., 2000), and it is coupled with

137 concentration of water-friendly aerosols.

138 The DeMott's parameterization scheme for determining the condensation and immersion freezing in the Thompson-

139 Eidhammer microphysics scheme was proposed in 2010 (DeMott et al., 2010, hereafter referred to as the DeMott2010

140 scheme) based on combined data from field experiments at a variety of locations over 14 years. In the Demott2010

141 parameterization, the relationship between the number concentration of aerosol-friendly aerosols and ice nucleating

142 particles (INP) is as follows:

143
$$n_{IN,T_k} = a(273.16 - T_k)^b n_{aero}^{(c(273.16-T_k)+d)} \qquad (1)$$

144 where n_{IN,T_k} is the INP number concentration at temperature of T_k; n_{aero} is the number concentration of ice-friendly

145 aerosols, and a, b, c, and d are constant coefficients equal to 5.94×10^{-5}, 3.33, 2.64×10^{-2}, and 3.33×10^{-3}, respectively.

146 The parameterization was tested with various temperatures and number concentration of ice-friendly aerosols, yielding

147 a good performance in reproducing ice crystal number concentration under conditions of relatively low mixing ratio

148 of water vapor or low concentration of INP compared with field–experimental data. The relationship between the

149 simulated number concentrations of ice-friendly aerosols and INP is basically linear for concentrations of both of

150 under 1,000 #/cm^3 (DeMott et al., 2010).

151 The above parameterization was further developed in 2015 (DeMott et al., 2015, hereafter the DeMott2015 scheme)

152 for conditions of higher mixing ratio of water vapor or higher concentrations of ice crystals based on the latest data

153 from field and laboratory experiments. According to the updated observational data, INP concentration increases

154 exponentially with number concentration of ice-friendly aerosols, and existing aerosols with relatively low

155 concentrations (less than 1,000 #/cm^3) can produce a large number of INP (more than 100,000 #/cm^3). The updated

156 relationship between the number concentrations of ice-friendly aerosols and INP in the DeMott2015 parameterization

157 scheme is as follows.

158
$$n_{IN,T_k} = c_f n_{aero}^{\alpha(273.16-T_k)+\beta} \exp(\gamma(273.16 - T_k) + \delta) \qquad (2)$$

159 where α, β, γ, and δ are constant coefficients equal to 0, 1.25, 0.46, and -11.6, respectively. The calibration factor c_f

160 ranges from 1 to 6, and is recommended to be 3.

161 The number concentration of INP produced by the DeMott2015 scheme is much higher than that produced by the

162 DeMott2010 scheme, and the difference grows larger with decreasing temperature and increasing number

163 concentration of ice-friendly aerosols (DeMott et al., 2015). Although the DeMott2015 scheme has been implemented

164   in the code of the Thompson-Eidhammer scheme, it cannot be used without modifying the code. Instead of using the

165   DeMott2010 scheme by default, we modified the code to call the DeMott2015 scheme in Thompson-Eidhammer

166   scheme for the condensation and immersion freezing in our simulations for investigating the ice nucleation involving

167   dust.

168   Originally, the calibration factor c_f is set to be 3; the threshold temperature is set to be –20 °C. For the ice nucleation

169   process in Thompson-Eidhammer scheme, the number concentrations of both water-friendly aerosols and ice-friendly

170   aerosols are pre-given in the initialization of the simulations, and are derived from the climatological data produced

171   by global model simulations in which particles and their precursors are emitted by natural and anthropogenic sources

172   and explicitly modeled with various size bins for multiple species of aerosols by the GOCART model. In the

173   consequent simulations, a fake aerosol emission is implemented by giving a variable lower boundary condition based

174   on the initial near-surface aerosol concentration and a simple mean surface wind for calculating a constant aerosol

175   flux at the lowest level in the model. The number concentrations of both water-friendly aerosols and ice-friendly

176   aerosols are then updated at every time step by summing up the fake aerosol emission fluxes and tendencies induced

177   by aerosol-cloud-interactions. The limitation of the current aerosol-aware Thompson-Eidhammer scheme is that the

178   aerosol profile generated from a fake emission cannot represent the realistic aerosol level all the time, especially over

179   areas with complex weathers, such as East Asia, leading to errors in quantifying the indirect effects of aerosols.

180   By coupling the GOCART aerosol model with the Thompson-Eidhammer microphysics scheme, it allows the model

181   to explicitly evaluate the indirect effect of natural-source aerosols on the basic of a relatively realistic emission

182   production, for instance, the effect of dust on ice nucleation during severe dust episodes or dust-intensive season.

183

184   **3 Implementation of GOCART-Thompson microphysics scheme**

185   To investigate the real-time indirect effects of dust aerosol over East Asia, a new treatment was implemented into

186   WRF-Chem to couple the GOCART aerosol model and the Thompson-Eidhammer microphysics scheme, namely

187   GOCART-Thompson microphysics scheme. To accomplish this, WRF-Chem version 3.8.1 has been modified in the

188   following three steps.

189

3.1 Upgraded GOCART aerosol model

Currently, the GOCART aerosol model generates only the mass concentration for aerosols but no number concentrations. However, the number concentrations of aerosols are required for a microphysics scheme to evaluate the indirect effects of aerosols. Therefore, modification was needed to provide information about the number concentrations of aerosols from the mass concentration produced in GOCART aerosol model.

The aerosol mass concentration was converted into number concentration using the aerosol density and effective radius for each size bin. Assuming that dust particles are spherical, the mass per dust particle (m_p, μg/#) for a size bin can be approximated through the mean effective radius (r_{dust}, m) and density (ρ_{dust}, kg/m^3) for that size bin.

$$m_p = \rho_{dust} \times \frac{4}{3} \times \pi r_{dust}^3 \tag{3}$$

The number concentration of dust particles N (#/kg) for size bin n at a grid point (i, j, k) is then calculated by the following equation:

$$N(i, j, k, n) = C(i, j, k, n)/ m_p \tag{4}$$

where $C(i, j, k, n)$ is the dust mass mixing ratio (μg/kg) for size bin n at grid point (i, j, k). Summing up the aerosol number concentrations through all of the size bins gives a total dust number concentration, which will be passed into the Thompson-Eidhammer microphysics scheme. Note that all of the dust particles are treated as ice-friendly aerosols in this study and represented by a newly-introduction variable, ice –friendly aerosol produced by GOCART aerosol model (*GNIFA*).

$$GNIFA(i, j, k) = \sum_{i=1}^{n} N(i, j, k, n) \tag{5}$$

3.2 GOCART-Thompson microphysics scheme

This part of modification was to hoop up the GOCART aerosol model and the Thompson-Eidhammer microphysics scheme.

212   Instead of reading in the pre-given climatological aerosol data, the initialization module of the Thompson-Eidhammer

213   microphysics scheme was modified to apply the bulk number concentration of ice-friendly aerosols produced by the

214   GOCART aerosol model for the calculation of the number concentration of ice nucleating particles.

215   After the microphysical processes are finished for a particular time step, the tendency of the bulk aerosol number

216   concentration (ten_{dust}, $\#/kg/s$) produced by the microphysics scheme is then passed into a wet scavenging scheme,

217   which will be described in detail in the following subsection, for the model to calculate the loss of aerosol mass due

218   to the microphysical processes within clouds, and update the aerosol mass field.

219

220   3.3 In-cloud wet scavenging

221   As no in-cloud scavenging is considered for dust aerosol in WRF-Chem, a new wet scavenging process was introduced

222   into WRF-Chem to calculate the loss of aerosol mass due to the microphysical processes within clouds using the

223   tendency of aerosol number concentration produced by the microphysics scheme. Assuming that the collection of dust

224   particles is proportional to the number concentration of dust particles, the fraction of dust particle for each size bin

225   (φ, $\%$) can be calculated in the GOCART aerosol model:

$$226 \qquad \varphi(i, j, k, n) = \frac{N(i,j,k,n)}{GNIFA(i,j,k)} \qquad (6)$$

227   The tendency of ice-friendly aerosol is then distributed into each size bin and the loss of dust mass due to the

228   microphysical processes (*wetscav*, $\mu g/kg$) for a particular size bin n is calculated by the following equation:

$$229 \qquad wetscav(i, j, k, n) = ten_{dust}\ (i, j, k) \times \varphi(i, j, k, n) \times m_p \times dt \qquad (7)$$

230   where dt is the time step for the simulation.

231   The mass mixing ratio (C, $\mu g/kg$) for dust aerosol in a particular size bin n is then updated at the next time step:

$$232 \qquad C_{(i,j,k,n)}^{t+1} = C_{(i,j,k,n)}^{t} - wetscav_{(i,j,k,n)}^{t} \qquad (8)$$

233   Apart from the in-cloud scavenging, the below-cloud wet removal is calculated by the default wet deposition scheme

234   in the GOCART aerosol model, in which the wet removal of dust is removed by a constant scavenging factor when

235   there is a precipitation (Duce et al., 1991;Hsu et al., 2009).

236

4 Model configurations

A numerical experiment was conducted to examine the performance of the newly-implemented GOCART–Thompson microphysics scheme in simulating the ice nucleation process induced by dust in the atmosphere. Two simulations were carried out for the numerical test. One control run (CTRL) was simulated without dust and one test run (DUST) with dust. According to the observations, the dust events in 2012 over East Asia were concentrated in mid-March to late-April, and the satellite observations from mid-March to the end of April were available for model validation; therefore, the simulation period was from March 9 to April 30, 2012, with the first eight days as "spin-up" time. Only the results from March 17 to April 30, 2012 were used for the analysis. The final reanalysis data provided by the United States National Center of Environmental Prediction with a horizontal resolution of one degree was used for generating the initial and boundary conditions for the meteorological fields, and the simulations were re-initialized every four days, with the aerosol field being re-cycled, which means that the output of the aerosol field from the previous four-day run was used as the initial aerosol state for the subsequent four-day run. The integration time step for the simulations was 90s.

Two nested domains were used for the simulations, as shown in Figure 1. The outer domain (domain 1) is in a horizontal resolution of 27 km and covers the entire East Asia region. The inner domain (domain 2) is in a horizontal resolution of 9 km and covers the entire central to East China. Both domains have 40 vertical layers, with the top layer at 50 hPa. The locations of the two major dust sources, the Taklimakan Desert (TD) and the Gobi Desert (GD), are marked in Figure 1.

In the GOCART-Thompson scheme, the deposition nucleation is determined by the Phillip's parameterization (Phillips et al., 2008), the freezing of deliquesced aerosols using the hygroscopic aerosol concentration is parameterized following Koop's parameterization scheme (Koop et al., 2000), and the condensation and immersion freezing is parameterized by the DeMott2015 ice nucleation scheme. The new wet scavenging scheme was used for in-cloud wet scavenging of aerosols due to microphysical processes. The GOCART aerosol model was applied to simulate aerosol processes (Ginoux et al., 2001;Ginoux et al., 2004) and produce the number concentration of dust particles in DUST. Shao's dust emission (Kang et al., 2011;Shao et al., 2011) with soil data from the United states Geological Survey (Soil Survey Staff, 1993), which have been demonstrated to have good performance in reproducing

263 dust emissions over East Asia, was used to generate dust emission in the simulations of TEST. The number

264 concentration of dust particles was then fed into the GOCART-Thompson microphysics scheme and treated as ice-

265 friendly aerosols for calculating the condensation and immersion freezing involving dust by DeMott2015

266 parameterization scheme. In addition, the pre-given climatological profiles applied in the original Thompson-

267 Eidhammer scheme (Thompson and Eidhammer, 2014) were used to provide the number concentration of water-

268 friendly aerosols for the freezing of deliquesced aerosols calculated by Koops's parameterization scheme to consider

269 the background indirect effect of aerosols on ice nucleation for both the simulations of both CTRL and DUST in this

270 study.

271 Other important physical and chemical parameterizations applied for the simulations are as follows. The Mellor–

272 Yamada–Janjic (MYJ) turbulent kinetic energy scheme was used for the planetary boundary layer parameterization

273 (Janjić, 2002, 1994); the moisture convective processes were parameterized by the Grell-Freitas scheme (Grell and

274 Freitas, 2014); the short-wave (SW) and long-wave (LW) radiation budgets were calculated by the Rapid Radiative

275 Transfer Model for General Circulation (RRTMG) SW and LW radiation schemes (Mlawer et al., 1997;Iacono et al.,

276 2008); the gravitational settling and surface deposition were combined for aerosol dry deposition calculation (Wesely,

277 1989); a simple washout method was used for the below-cloud wet deposition of aerosols (Duce et al., 1991;Hsu et

278 al., 2006); and the aerosol optical properties were calculated based on the volume-averaging method (Horvath, 1998).

279

280 **5 Observations**

281 **5.1 Surface PM_{10} observations**

282 The hourly observations of surface concentration of particulate matter with diameter smaller than 10 μm (PM_{10}) at ten

283 environmental monitoring stations located in or surrounding the dust source areas in East Asia were used to examine

284 the capability of the model in reproducing dust levels at the ground surface during the simulation period. The ten

285 stations (indicated by blue dots in Figure 1) were located in the following five cities:Jinchang, Gansu Province,

286 Yinchuan, Qinghai Province, Shizuishan, Ningxia Province, Baotou, Inner Mongolia, and Yan'an, Shaanxi Province,

287 with two stations in each city.

288

12

289   **5.2 AERONET AOD observations**

290   The AERONET program is a ground-based aerosol remote sensing network for measuring aerosol optical properties

291   at sites distributed around the globe. This program provides a long-term database of aerosol optical properties such as

292   aerosol extinction coefficient, single-scattering albedo, and aerosol optical depth (AOD) measured at various

293   wavelength. The observational data from two sites were available for comparison with the simulation results during

294   the simulation period in this study. One was Dalanzadgad located to the north of the Gobi Desert in Mongolia, and

295   the other was the Semi-Arid Climate and Environment Observatory of Lanzhou University (SACOL) located at

296   Lanzhou, Gansu Province, China. The exact locations of the two AERONET sites are depicted by the red triangles in

297   Figure 1. All of the measured data had passed the quality control standard level 2, with an uncertainty of ±0.01 (Holben

298   et al., 2001).

299

300   **5.3 Satellite data**

301   **5.3.1 Multi-angle Imaging SpectroRadiometer (MISR)**

302   The MISR instrument aboard the Terra platform of the United State National Aeronautics and Space Administration

303   (NASA) has been monitoring aerosol properties globally since 2000. It measures the aerosol properties in four narrow

304   spectral band centered at 443 nm, 555 nm, 670 nm, and 865 nm, due to which the aerosol properties even over highly

305   bright surfaces, such as deserts, can be retrieved (Martonchik et al., 2004;Diner et al., 1998). In this study, the AOD

306   data at 555 nm retrieved from the MISR level 3 products with a spatial resolution of 0.5° were used for comparison

307   with the spatial distribution of simulated AOD over East Asia during the investigated period.

308

309   **5.3.2 Moderate Resolution Imaging Spectroradiometer (MODIS)**

310   The MODIS instruments aboard Terra and Aqua platforms of NASA monitor Earth's surface and provide global high-

311   resolution cloud and aerosol optical properties at a near-daily interval (Kaufman et al., 1997).

312   To retrieve aerosol information over bright surfaces, the Deep Blue algorithm was developed to employ retrievals

313   from the blue channels of the MODIS instruments, at which wavelength the surface reflectance is very low, such that

13

314　the presence of aerosol can be detected by increasing total reflectance and enhanced spectral contrast (Hsu et al., 2006).

315　By applying this algorithm, the AOD values at wavelengths of 214 nm, 470 nm, 550 nm, and 670 nm over bright

316　surfaces can be retrieved. In this study, the MODIS level 2 AOD data at 550 nm with a spatial resolution of 10 km

317　were used for comparison with the simulated AOD during the simulation period.

318

319　**5.3.3 Cloud-Aerosol Lidar and Infrared Pathfinder Satellite Observation (CALIPSO)**

320　The Cloud-Aerosol Lidar and Infrared Pathfinder Satellite, which is aboard the Aqua platform of NASA, combines

321　an active Light Detection and Ranging (LIDAR) instrument with passive infrared and visible imagers to probe the

322　vertical structure and properties of thin clouds and aerosols around the globe (Vaughan et al., 2004). It aims to fill

323　existing gaps in the ability to measure the global distribution of aerosols and cloud properties, and provides three-

324　dimensional perspectives of how clouds and aerosols form, evolve, and affect weather and climate. It measures high-

325　resolution vertical profiles of aerosol and cloud extinction coefficient globally at wavelengths of 532nm and 1064 nm.

326　The atmospheric IWC is derived from the observational cloud extinction coefficients at 532 nm (Winker et al., 2009).

327　In this study, the vertical profiles of CALIPSO IWC with a horizontal resolution of 5 km and vertical resolution of 60

328　m were applied to verify the performance of the model in simulating the vertical distribution of atmospheric IWC.

329

330　**6 Results and model validation**

331　**6.1 Dust over East Asia**

332　The time series of daily average dust load over the entire East Asia region (domain 1) during the simulation period is

333　shown in Figure 2a. In total four dust events occurred during the simulation period, lasting from March 18 to 25,

334　March 30 to April 7, April 9 to 19, and April 22 to 29, 2012. The case from April 22 to 29 was the most significant

335　one, with daily dust load that double as the other cases. The fraction of daily dust load for each size bin is also shown

336　in Figure 2a. The dust particles in the fourth and fifth bins with effective diameters ranging from 6 to 20 μm account

337　for the major part (around 60%) of the total mass of dust aerosols.

338   The number concentrations of dust particles over East Asia were vertically integrated to obtain the number density of

339   dust particles. As shown in Figure 2b, the time series of the daily average number density of dust particles over East

340   Asia during the simulation period shows a similar distribution as that for dust load; the noteworthy distinction between

341   the two time series lies in the fraction of each size bin. The two size bins with the smallest diameters (no larger than

342   3.6 μm) account for over 80% of the total number of dust particles, and the particles with diameters smaller than 6 μm

343   account for over 95% of the total number of dust particles, indicating that the smallest dust particles are the main

344   source of ice-friendly aerosol to serve as IN in the atmosphere.

345

346   **6.1.1 Surface PM$_{10}$ concentration**

347   To evaluate the performance of WRF-Chem in reproducing dust emissions over East Asia, the simulated surface PM$_{10}$

348   concentrations were compared with the observations from the ten environmental monitoring stations located near dust

349   sources and downwind areas (described in Section 5.1). The time series of the observed and simulated surface PM$_{10}$

350   concentrations during the simulation period are shown in Figure 3. Note that the simulated PM$_{10}$ concentrations were

351   extracted from the nearest grid point to the geographical coordinates of the stations. The stations in the same city were

352   assigned into one group, such that there were five groups in Figure 3. Overall, the model shows a good performance

353   in simulating the dust cycle at different locations, with evolution and magnitude of the daily mean PM$_{10}$ concentration

354   well captured at most of the stations. The model tends to produce lower surface PM$_{10}$ concentration than those

355   observed, as no other emissions were considered in the simulations apart from dust. However, the dust events on

356   March 21 and April 26 were overestimated by the model at both stations in Shizuishan (Figure 3c and d) and Yinchuan

357   (Figure 3i and j).

358   The performance statistics were computed from the daily average simulated PM$_{10}$ concentration from DUST and the

359   corresponding observations, as shown in Table 1. The model tends to produce lower surface PM$_{10}$ concentrations than

360   those observed, as no other emissions were considered in the simulations. The mean bias (MB) ranged from -108.73

361   μg/m^3 to 72.46 μg/m^3, with a mean over all the stations of -18.84 μg/m^3. The mean error (ME) ranged from 46.07

362   μg/m3 to 155.83 μg/m3, with a mean over all of the stations of 107.24 μg/m^3. The root mean squared error (RMSE)

363   ranged from 64.78 μg/m^3 to 317.73 μg/m^3, with a mean over all of the stations of 181.28 μg/m^3. The relatively large

364   values of the MB, ME and RMSE are mainly attributed to the fact that no other aerosol emissions were considered in

15

365   the simulations other than dust, while the surface PM_{10} concentration at the monitoring stations is influenced by

366   aerosols emitted from other sources, such as anthropogenic emissions. The correlation coefficient (r) ranged from 0.59

367   to 0.87, with an average for all of the stations of 0.70. The comparisons between the observed and simulated surface

368   PM_{10} concentration indicates that the model is capable of reproducing the surface dust concentration reasonably during

369   dust events over East Asia.

370

371   **6.1.2 AOD time series**

372   To examine the performance of the model in reproducing the column sum of dust in the atmosphere, the simulated

373   AOD values were compared with observations measured at two AERONET sites during the simulation period, as

374   shown in Figure 4.

375   The site at Dalanzadgad (Figure 4a) is located in Mongolia to the north of the Gobi Desert. Overall, the evolution and

376   magnitude of the AOD time series at Dalanzadgad were reasonably reproduced by the model during the simulation

377   period, despite the fact that the simulated AOD was overestimated at the end of March and in mid-April compared to

378   the observed values.

379   SACOL (Figure 4b) is a site located in Lanzhou, Gansu Province, which is a typical downwind area for dust in China.

380   The model showed a good performance in reproducing the time series of AOD at SACOL during the entire simulation

381   period, with evolution and magnitude of AOD well captured.

382

383   **6.1.3 AOD spatial distribution**

384   The spatial distribution of monthly mean simulated AOD was also compared with observed values from MODIS and

385   MISR products in Figure 5. Note that the high AOD values observed at North, East, South China and part of Southeast

386   Asia are attributed to the abundant anthropogenic emissions, while those high values in the circle area are mostly due

387   to dust events. The region with high AOD values in the west part of the circled area is TD, and the region with

388   relatively lower AOD in the east part of the circled area is GD. The AOD observed by MODIS showed high values at

389   the dust source region in both March and April of 2012, as shown in Figures 5a and b. The mean observed AOD over

390   GD was lower than that over TD in both March and April, and the mean observed AOD was higher in April than in

391   March over both dust source areas. The spatial patterns of AOD observed by MISR are similar to MODIS, with

392   comparable mean values over GD. However, the mean AOD values over TD observed by MISR are 36% and 40%

393   lower than those by MODIS in March and April, respectively (Figure 5c and d).

394   The spatial patterns for the mean simulated AOD were similar to the observed values in both months but closer to

395   those from MODIS, as shown in Figures 5e and f. The model shows a good capability in capturing the spatial

396   characteristics of the AOD over the dust source areas. For example, the mean observed AOD was higher in the

397   southern part of TD than that in the northern part in March, and showed an increase from March to April over GD,

398   both of which were captured by the model. The values of the mean simulated AOD over the Gobi Desert (0.33 for

399   March and 0.39 for April) are comparable to the observational values from both MODIS (0.30 for March and 0.32 for

400   April) and MISR (0.31 for March and 0.34 for April), but the mean simulated AOD over TD (0.54 for March and 0.64

401   for April) are between the values of the MISR observations (0.72 for March and 0.88 for April) and the MODIS

402   observations (0.46 for March and 0.53 for April).

403   In summary, it was demonstrated that the dust emissions simulated by WRF-Chem are reliable for further analysis by

404   the comparison between the simulation results and the observations for surface PM_{10} concentrations, as well as the

405   temporal and spatial distributions of AOD values.

406

407   **6.2 Cloud ice over East Asia**

408   Dust particles are effective IN and play an important role in ice nucleation in the atmosphere under appropriate

409   conditions. With the large number of IN served by dust particles emitted into the atmosphere, an increase in the number

410   of ice crystals is expected in the results from DUST compared with those from CTRL, after taking into account the

411   effects of dust particles in the GOCART–Thompson microphysics scheme. Figure 6 shows the overall comparison

412   between the simulated cloud ice mixing ratio and ice crystal number concentration at each simulated data point (at

413   all model grids at hourly intervals) from CTRL and DUST during the entire simulation period.

414   As expected, the model produces a much higher cloud ice mixing ratio (Figure 6a) and ice crystal number

415   concentration (Figure 6b) in DUST. The simulated cloud ice mixing ratio produced in CTRL is lower than 2 μg/kg at

416 most data points during the simulation period, whereas the data points with simulated ice mixing ratio higher than 2

417 μg/kg are substantially increased in the output of DUST. Similarly, the simulated ice crystal number concentration

418 produced in CTRL is lower than 0.5×10^6 #/kg at most data points during the simulation period, by contrast, the

419 simulated ice crystal number concentration number concentration is higher than 0.5×10^6 #/kg at over a half of total

420 data points in DUST. The substantial increase of simulated cloud ice mixing ratio and ice crystal number concentration

421 indicates that the enhancement of ice nucleation process induced by dust is successfully reproduced by the newly-

422 implemented GOCART-Thompson microphysics scheme during the simulation period. +

423

424 **6.2.1 Spatial distribution of ice water path (IWP)**

425 The spatial distributions of the simulated IWP and ice crystal number density from CTRL and DUST in Figure 7

426 further demonstrate the enhancement in cloud ice due to dust over East Asia. The IWP produced by CTRL was

427 relatively high over west and east China, as well as at the south boundary of the simulation domain, with the values

428 as high as 20 g/m^2 (Figure 7a). After considering the effect of dust in the ice nucleation process, the IWP produced by

429 DUST increased substantially over dust sources and downwind areas (Figure 7b and c), with values higher by 5-10

430 g/m^2. The mean IWP averaged over the domain during the simulation period was 9.33 g/m^2 for DUST, and 7.95 g/m^2

431 for CTRL. As shown in Figures 7d–f, the spatial pattern for the enhancement of ice crystal number density over East

432 Asia was similar with that for the IWP. The mean ice crystal number density averaged over the domain during the

433 simulation period was 2.91×10^8 /m^2 for DUST, and 2.76×10^8 /m^2 for CTRL.

434 The mean IWP and ice crystal number density were increased by 15% and 8% over vast areas of East Asia upon

435 considering the effect of dust in the ice nucleation process in the simulation, and such effect can reach as far as the

436 open ocean of the Western Pacific (Figure 7b and 7e), as the outbreak of cold high system over northeast Asia can

437 bring quantitative dust aerosol down to the Western Pacific or even further during dust season..

438

439 **6.2.2 IWC during dust events**

440 The vertical profile of the simulated IWC was also compared with the observation from CALIPSO during dust events.

441 As mentioned in section 5.1, a total of four dust events occurred during the simulation period, lasting from March 18

18

442   to 25, March 30 to April 7, April 9 to 19, and April 22 to 28, 2012. As shown in Figures 8 and 9, the performance of

443   the model in simulating the vertical profile of IWC was evaluated by comparing the observations measured at 06 UTC

444   on March 21, 18 UTC on April 1, 18 UTC on April 9, and 05 UTC on April 23, 2012 with the simulated profiles at

445   the same hour.

446   CALIPSO measures the global distribution of aerosol and cloud properties by LIDAR, which uses a laser to generate

447   visible light with a wavelength of 1 μm or less to detect small particles or droplets in the atmosphere. Therefore,

448   CALIPSO instruments are more sensitive to tenuous ice clouds and liquid clouds composed of small particles or

449   droplets, which are invisible to instruments using signals of near-infrared or infrared wavelength to detect clouds.

450   Moreover, the LIDAR signal is attenuated rapidly in optically dense clouds that the infrared or near-infrared signals

451   can easily penetrate(Winker et al., 2010). As a result, the CALIPSO observations of IWC are mostly at the locations

452   where the temperatures is lower than −40 °C and the altitude is greater than 6 km poleward to 12 km equatorward,

453   and mostly those without precipitating ice. Given the above considerations, the simulated IWC profiles compared with

454   the CALIPSO observations are referred to as only cloud ice in this section.

455   The simulated dust load over East Asia at 06 UTC on March 21, 2012 is shown in Figure 8a, in which the dust covered

456   vast areas from West to East China between 35°N and 45°N, and the orbit of the satellite passed through the area with

457   heavy dust load at around 100°E. Along the satellite orbit, the abundant dust particles were transported to as high as

458   10 km aloft (Figure 8c). At this time, a high concentration of IWC was observed along the satellite orbit at an altitude

459   of around 10 km between 30°N and 45°N (Figure 8e). The simulation result from CTRL (Figure 8g) shows that the

460   model produces some ice cloud at altitude of 9–10 km between 35°N and 45°N, but with much lower IWC compared

461   to the observations. Nevertheless, by considering the effect of dust on ice nucleation process in DUST, it results in a

462   much higher IWC at altitude of 9–10 km between 35°N and 45°N (Figure 8i), which is much more consistent with the

463   observations. The comparison between the simulation results from CTRL and DUST indicates that the high IWC

464   observed by the satellite between 30°N and 35°N might be unrelated to microphysical processes, but instead due to

465   strong convective motions over South China.

466   On April 1, 2012, Central to East China was covered by a thick dust plume, and the orbit of the satellite passed between

467   25°N and 43°N along 120°E at 18 UTC (Figure 8b). Dust particles were distributed vertically from the surface to over

468   8 km along the satellite orbit (Figure 8d). A band of high IWC was observed by the satellite at altitude of 5 km to 10

469   km between 33°N and 44°N (Figure 8f), which was highly underestimated in the results of the CTRL run without dust.

470   In contrast, the observed band of high IWC was reproduced by the model in DUST with much more consistent

471   magnitude (Figure 8j).

472   At 18 UTC on April 9, 2012, the satellite was scanning the dust source over GD, which was covered by a thick dust

473   plume between 35°N and 45°N (Figure 10a), with dust particles lifted up to 10 km above the surface (Figure 9c). High

474   concentration of IWC was observed by the satellite at altitude from 5 km to 11 km between 30°N and 45°N (Figure

475   9e). In this case, the model reproduced the high concentration of IWC at the observed location in the results from both

476   CTRL and DUST, although the IWC was significantly underestimated in the results from CTRL (Figure 9g), while it

477   was better reproduced in the results from DUST (Figure 9j).

478   Similar to the previous cases, the satellite was scanning along east coast of China at 05 UTC on April 23, 2012, when

479   a dust plume was arriving from the dust sources and affecting areas between 35°N and 45°N (Figure 9b), and dust

480   particles were distributed vertically from the surface to 10 km along the scanning track of the satellite (Figure 9d).

481   Along the orbit of the satellite, a band of high IWC areas was observed at altitudes between 5 km and 12 km from

482   30°N to 45°N (Figure 9f). In the results from CTRL, the model reproduced the high-IWC values at the correct locations,

483   but with substantially lower values (Figure 9h); however, upon taking into account the effect of dust in the GOCART-

484   Thompson microphysics scheme, the high-IWC areas were well reproduced by the model, with much more consistent

485   values (Figure 9j).

486   By comparing the satellite-observational and simulated vertical profiles of IWC during the various dust events, it was

487   demonstrated that the model reproduces the enhancement of IWC clouds in the mid- to upper troposphere by taking

488   in to account the effect of dust in the ice nucleation process, which substantially improves the simulation of cloud ice.

489

490   **6.2.3 Mean vertical profiles of IWC**

491   The mean profiles of the observed IWC, as well as the simulated IWC from CTRL and DUST for the four dust events

492   discussed in Section 6.2.2, are shown in Figure 10. Note that the "mean profile" of IWC is the average over the

493   available data points for the IWC along the orbit of the satellite between 30°N to 45°N for each of the dust events

494   shown in Figures 8 and 9.

495   Compared with the results from CTRL, the vertical profile of the simulated IWC was substantially improved in DUST

496   for each dust event, with the enhancement of the ice nucleation process well captured by the GOCART-Thompson

497   microphysics scheme. However, there were still discrepancies between observations and the simulation results from

498   DUST, the magnitudes of the vertical IWC produced by the model were always lower than the observed values.

499   For the cases on March 21 and April 1, the peaks of IWC were observed at 9.5 km and 8 km, respectively, whereas

500   the simulated peak of IWC were located at 7 km and 7.5 km, respectively, with lower peak values. The lower peak

501   value for the case on March 21 was due to the missing of the high IWC observed between 30°N to 45°N in the

502   simulation results (Figure 8e and i), while the lower peak value for the case on April 1 was due to the underestimation

503   of the IWC around 35°N (Figure 8f and j). The locations of the peaks of simulated IWC for the cases on April 9 and

504   April 23 were more consistent with the observed peaks, but still possessed lower values due to the missing or

505   underestimation of high IWC with respect to the observations.

506

6.3 Sensitivity test and discussion

508   As discussed in Section 6.2.3, the simulation of cloud ice is greatly improved by considering the enhancement of ice

509   nucleation process induced by dust, which is well captured by the GOCART–Thompson microphysics scheme.

510   However, the IWC is still underestimated by the model during dust events. To determine the reason for this limitation,

511   numerical experiments were performed to investigate the sensitivity of simulated IWC to the parameters of the ice

512   nucleation parameterization in the GOCART–Thompson microphysics scheme.

513

6.3.1 Calibration factor c_f

515   The calibration factor c_f is an empirical tuning coefficient derived from observational data from field and laboratory

516   experiments. It ranges from 1 to 6, and recommended to be 3 (DeMott et al., 2015), which was applied in the previous

517   simulations. Three other experiments were conducted to investigate the sensitivity of the simulated IWC to c_f values

518   ranging from 3 to 6.

519   The mean profiles of IWC from simulation results were compared with the CALIPSO observations for the dust events

520   discussed in Section 6.2.2 and 6.2.3, as shown in Figure 11. For the cases on March 21 and April 1, changing c_f did

521   not result in an increase of IWC; instead, the simulated IWC remained consistent for c_f values varying from 3 to 6.

522   For the case on April 9, the simulated IWC increased between 6 km and 9 km and was higher and closer to the observed

523   profile when c_f was equal to 5 and 6 compared to the case when c_f was set to 3 and 4.

524   For the case on April 23, two peaks were observed in the profiles of simulated IWC, located at 7 km and 10 km. By

525   increasing c_f values from 3 to 6, the simulated IWC remained unchanged for the peak at 10 km, but gradually

526   increased for the peak at 7 km. The peak of the simulated IWC at 7 km should correspond to the observed peak

527   between 6 km to 8 km, which was slightly overestimated by the model.

528   In summary, increasing the calibration factor c_f from 3 to 6 does not necessarily lead to a significant variation in the

529   simulated IWC during dust events, and the model achieves a relatively better performance in reproducing the profile

530   of IWC when the c_f is set to 5.

531   As ice nucleation occurs only in a super-saturated atmosphere with respect to water vapor, the ice nucleation process

532   would be terminated in the GOCART-Thompson microphysics scheme when the environmental RH_i is lower than the

533   threshold RH_i, which was set to 105% for the simulations in this study. The consistency in the simulated IWC with

534   increasing c_f for the cases in Figure 11 indicates that in these cases, the environmental RH_i had already reached below

535   105% when c_f was set to 3, meaning that the water vapor available for freezing into ice crystals has been consumed

536   up with c_f equal to 3, therefore, increasing c_f could not lead to a further increase in simulated IWC. Given the above,

537   lowering the threshold RH_i might result in an enhancement of the ice nucleation process as well as the simulated IWC,

538   which will be discussed in the following section.

539

540   **6.3.2 Threshold of relative humidity**

541   In this study, the threshold relative humidity to trigger the ice nucleation process in the simulation was originally set

542   to 105%, which was selected for the central lamina condition in the laboratory experiments to derive the DeMott2015

543   ice nucleation scheme (DeMott et al., 2015). However, as reported in other studies, the number of ice nucleating

544 particles starts to rise when the relative humidity exceeds 100% (DeMott et al., 2011). Therefore, a sensitivity

545 experiment was carried out to investigate the response of simulated IWC to lower threshold relative humidity.

546 The mean profiles of IWC from the simulation results were compared with the CALIPSO observations for the

547 aforementioned dust events, as shown in Figure 12. With the threshold relative humidity lowered to 100%, the

548 simulated IWC showed an increase throughout the vertical profile with the most significant increase at the peaks,

549 suggesting more consistency with the observations for all of the dust events, except the one on April 1. In the case on

550 April 1, the simulated IWC increased at lower altitudes than the observed peak, but slightly decreased right at the peak

551 with lowering the threshold relative humidity to 100%. Overall, the simulation of IWC during dust events was

552 significantly improved by lowering the threshold relative humidity from 105% to 100%.

553

554 **7 Conclusions**

555 A new treatment, the GOCART–Thompson scheme, was implemented into WRF-Chem to couple the GOCART

556 aerosol model to the aerosol-aware Thompson-Eidhammer microphysics scheme. By applying this newly-

557 implemented microphysics scheme, the effect of dust on the ice nucleation process by serving as IN in the atmosphere

558 can be quantified and evaluated. Numerical experiments, including a control run without dust and a test run with dust,

559 were then carried out to evaluate the performance of the newly–implemented GOCART–Thompson microphysics

560 scheme in simulating the effect of dust on the content of cloud ice over East Asia during a typical dust-intensive period,

561 by comparing the simulation results with various observations.

562 Based on the GOCART aerosol model the model reproduced dust emission reasonably well, by capturing the evolution

563 and magnitude of surface PM_{10} concentration at the locations of various environmental monitoring stations and the

564 AOD at two AERONET sites. The spatial patterns of the mean AOD over East Asia during the simulation period were

565 also consistent with satellite observations.

566 The effect of dust on the ice nucleation process was then quantified and evaluated in the GOCART–Thompson

567 microphysics scheme. Upon considering the effect of dust in the simulation, the simulated ice water mixing ratio and

568 ice crystal number concentration over East Asia were 15% and 7% higher than those simulated without dust, with the

569 most significant enhancements located over dust source regions and downwind areas.

570   Comparison between the vertical profiles of the satellite-observed and simulated IWC during various dust events

571   indicated that the enhancement of cloud ice induced by abundant dust particles serving as IN is well captured by the

572   GOCART–Thompson microphysics scheme, with the results from the simulation with dust much more consistent with

573   the satellite–observations, although the IWC is generally underestimated by the model.

574   Sensitivity experiments revealed that the simulated IWC was not very sensitive to the calibration factor defined in the

575   DeMott2015 ice nucleation scheme, but the model delivered a slight better performance in reproducing the IWC when

576   the calibration factor was set to 5. However, the simulated IWC was sensitive to the threshold relative humidity to

577   trigger the ice nucleation process in the model and was improved upon lowering the threshold relative humidity from

578   105% to 100%.

579

591

592   **References**

593   Atkinson, J. D., Murray, B. J., Woodhouse, M. T., Whale, T. F., Baustian, K. J., Carslaw, K. S., Dobbie, S.,

594   O'sullivan, D., and Malkin, T. L.: The importance of feldspar for ice nucleation by mineral dust inmixed-

595   phase clouds, Nature, 498, 355, 2013.

596   Baró, R., Jiménez-Guerrero, P., Balzarini, A., Curci, G., Forkel, R., Grell, G., Hirtl, M., Honzak, L., Langer,

597   M., and Pérez, J. L.: Sensitivity analysis of the microphysics scheme in WRF-Chem contributions to

598   AQMEII phase 2, Atmospheric Environment, 115, 620-629, 2015.

599   Bi, J., Huang, J., Fu, Q., Ge, J., Shi, J., Zhou, T., and Zhang, W.: Field measurement of clear-sky solar

600   irradiance in Badain Jaran Desert of Northwestern China, Journal of Quantitative Spectroscopy and

601   Radiative Transfer, 122, 194-207, 2013.

602   Chapman, E. G., Gustafson Jr, W., Easter, R. C., Barnard, J. C., Ghan, S. J., Pekour, M. S., and Fast, J. D.:

603   Coupling aerosol-cloud-radiative processes in the WRF-Chem model: Investigating the radiative impact of

604   elevated point sources, Atmospheric Chemistry and Physics, 9, 945-964, 2009.

605   Chin, M., Rood, R. B., Lin, S.-J., Müller, J.-F., and Thompson, A. M.: Atmospheric sulfur cycle simulated

606   in the global model GOCART: Model description and global properties, 2000.

607   DeMott, P. J., Sassen, K., Poellot, M. R., Baumgardner, D., Rogers, D. C., Brooks, S. D., Prenni, A. J., and

608   Kreidenweis, S. M.: African dust aerosols as atmospheric ice nuclei, Geophysical Research Letters, 30,

609   2003.

610   DeMott, P. J., Prenni, A. J., Liu, X., Kreidenweis, S. M., Petters, M. D., Twohy, C. H., Richardson, M.,

611   Eidhammer, T., and Rogers, D.: Predicting global atmospheric ice nuclei distributions and their impacts on

612   climate, Proceedings of the National Academy of Sciences, 107, 11217-11222, 2010.

613   DeMott, P. J., Möhler, O., Stetzer, O., Vali, G., Levin, Z., Petters, M. D., Murakami, M., Leisner, T.,

614   Bundke, U., and Klein, H.: Resurgence in ice nuclei measurement research, Bulletin of the American

615   Meteorological Society, 92, 1623-1635, 2011.

616   DeMott, P. J., Prenni, A. J., McMeeking, G. R., Sullivan, R. C., Petters, M. D., Tobo, Y., Niemand, M.,

617   Möhler, O., Snider, J. R., and Wang, Z.: Integrating laboratory and field data to quantify the immersion

618   freezing ice nucleation activity of mineral dust particles, Atmospheric Chemistry and Physics, 15, 393-409,

619   2015.

620   Diner, D. J., Barge, L. M., Bruegge, C. J., Chrien, T. G., Conel, J. E., Eastwood, M. L., Garcia, J. D.,

621   Hernandez, M. A., Kurzweil, C. G., and Ledeboer, W. C.: The Airborne Multi-angle Imaging

622   SpectroRadiometer (AirMISR): instrument description and first results, IEEE Transactions on Geoscience

623   and Remote Sensing, 36, 1339-1349, 1998.

624   Duce, R., Liss, P., Merrill, J., Atlas, E., Buat-Menard, P., Hicks, B., Miller, J., Prospero, J., Arimoto, R.,
625   and Church, T.: The atmospheric input of trace species to the world ocean, Global biogeochemical cycles,
626   5, 193-259, 1991.

627   Ge, J., Su, J., Ackerman, T., Fu, Q., Huang, J., and Shi, J.: Dust aerosol optical properties retrieval and
628   radiative forcing over northwestern China during the 2008 China-US joint field experiment, Journal of
629   Geophysical Research: Atmospheres, 115, 2010.

630   Ginoux, P., Chin, M., Tegen, I., Prospero, J. M., Holben, B., Dubovik, O., and Lin, S. J.: Sources and
631   distributions of dust aerosols simulated with the GOCART model, Journal of Geophysical Research:
632   Atmospheres, 106, 20255-20273, 2001.

633   Ginoux, P., Prospero, J. M., Torres, O., and Chin, M.: Long-term simulation of global dust distribution with
634   the GOCART model: correlation with North Atlantic Oscillation, Environmental Modelling & Software,
635   19, 113-128, 2004.

636   Grell, G., Peckham, S., Fast, J., Singh, B., Easter, R., Gustafson, W., Rasch, P., Wolters, S., Barth, M., and
637   Pfister, G.: WRF-Chem V3. 5: A summary of status and updates, EGU General Assembly Conference
638   Abstracts, 2013, 11332.

639   Grell, G. A., and Freitas, S. R.: A scale and aerosol aware stochastic convective parameterization for
640   weather and air quality modeling, Atmos. Chem. Phys, 14, 5233-5250, 2014.

641   Hansen, J., Sato, M., and Ruedy, R.: Radiative forcing and climate response, Journal of Geophysical
642   Research: Atmospheres, 102, 6831-6864, 1997.

643   Hartmann, D., Tank, A., and Rusticucci, M.: IPCC fifth assessment report, climate change 2013: The
644   physical science basis, IPCC AR5, 31-39, 2013.

645   Holben, B., Tanre, D., Smirnov, A., Eck, T., Slutsker, I., Abuhassan, N., Newcomb, W., Schafer, J.,
646   Chatenet, B., and Lavenu, F.: An emerging ground-based aerosol climatology: Aerosol optical depth from
647   AERONET, Journal of Geophysical Research: Atmospheres, 106, 12067-12097, 2001.

648   Hoose, C., Lohmann, U., Erdin, R., and Tegen, I.: The global influence of dust mineralogical composition
649   on heterogeneous ice nucleation in mixed-phase clouds, Environmental Research Letters, 3, 025003, 2008.

650   Horvath, H.: Influence of atmospheric aerosols upon the global radiation balance, Atmospheric particles, 5,
651   62-63, 1998.

652   Hsu, N. C., Tsay, S.-C., King, M. D., and Herman, J. R.: Deep blue retrievals of Asian aerosol properties
653   during ACE-Asia, IEEE Transactions on Geoscience and Remote Sensing, 44, 3180-3195, 2006.

654   Hsu, S. C., Liu, S. C., Arimoto, R., Liu, T. H., Huang, Y. T., Tsai, F., Lin, F. J., and Kao, S. J.: Dust
655   deposition to the East China Sea and its biogeochemical implications, Journal of Geophysical Research:
656   Atmospheres, 114, 2009.

657   Huang, J., Fu, Q., Su, J., Tang, Q., Minnis, P., Hu, Y., Yi, Y., and Zhao, Q.: Taklimakan dust aerosol

658   radiative heating derived from CALIPSO observations using the Fu-Liou radiation model with CERES

659   constraints, Atmospheric Chemistry and Physics, 9, 4011-4021, 2009.

660   Huang, J.: Emission, transport, and radiative effects of mineral dust from the Taklimakan and Gobi deserts:

661   comparison of measurements and model results, Atmos. Chem. Phys, 1680, 7324, 2017.

662   Iacono, M. J., Delamere, J. S., Mlawer, E. J., Shephard, M. W., Clough, S. A., and Collins, W. D.: Radiative

663   forcing by long-lived greenhouse gases: Calculations with the AER radiative transfer models, Journal of

664   Geophysical Research: Atmospheres, 113, 2008.

665   Janjić, Z. I.: The step-mountain eta coordinate model: Further developments of the convection, viscous

666   sublayer, and turbulence closure schemes, Monthly Weather Review, 122, 927-945, 1994.

667   Janjić, Z. I.: Nonsingular implementation of the Mellor–Yamada level 2.5 scheme in the NCEP Meso model,

668   NCEP office note, 437, 61, 2002.

669   Kang, J. Y., Yoon, S. C., Shao, Y., and Kim, S. W.: Comparison of vertical dust flux by implementing three

670   dust emission schemes in WRF/Chem, Journal of Geophysical Research: Atmospheres, 116, 2011.

671   Karydis, V., Kumar, P., Barahona, D., Sokolik, I., and Nenes, A.: On the effect of dust particles on global

672   cloud condensation nuclei and cloud droplet number, Journal of Geophysical Research: Atmospheres, 116,

673   2011.

674   Kaufman, Y., Tanré, D., Remer, L. A., Vermote, E., Chu, A., and Holben, B.: Operational remote sensing

675   of tropospheric aerosol over land from EOS moderate resolution imaging spectroradiometer, Journal of

676   Geophysical Research: Atmospheres, 102, 17051-17067, 1997.

677   Koehler, K., Kreidenweis, S., DeMott, P., Petters, M., Prenni, A., and Möhler, O.: Laboratory investigations

678   of the impact of mineral dust aerosol on cold cloud formation, Atmospheric Chemistry and Physics, 10,

679   11955-11968, 2010.

680   Koop, T., Luo, B., Tsias, A., and Peter, T.: Water activity as the determinant for homogeneous ice

681   nucleation in aqueous solutions, Nature, 406, 611-614, 2000.

682   Lacis, A.: Climate forcing, climate sensitivity, and climate response: A radiative modeling perspective on

683   atmospheric aerosols, Aerosol forcing of climate, 11-42, 1995.

684   Liu, Huang, J., Shi, G., Takamura, T., Khatri, P., Bi, J., Shi, J., Wang, T., Wang, X., and Zhang, B.: Aerosol

685   optical properties and radiative effect determined from sky-radiometer over Loess Plateau of Northwest

686   China, Atmospheric Chemistry and Physics, 11, 11455-11463, 2011a.

687   Liu, Zheng, Y., Li, Z., Flynn, C., Welton, E. J., and Cribb, M.: Transport, vertical structure and radiative

688   properties of dust events in southeast China determined from ground and space sensors, Atmospheric

689   environment, 45, 6469-6480, 2011b.

690   Lohmann, U., and Diehl, K.: Sensitivity studies of the importance of dust ice nuclei for the indirect aerosol

691   effect on stratiform mixed-phase clouds, Journal of the Atmospheric Sciences, 63, 968-982, 2006.

692   Mallet, M., Tulet, P., Serça, D., Solmon, F., Dubovik, O., Pelon, J., Pont, V., and Thouron, O.: Impact of

693   dust aerosols on the radiative budget, surface heat fluxes, heating rate profiles and convective activity over

694   West Africa during March 2006, Atmospheric Chemistry and Physics, 9, 7143-7160, 2009.

695   Martonchik, J., Diner, D., Kahn, R., Gaitley, B., and Holben, B.: Comparison of MISR and AERONET

696   aerosol optical depths over desert sites, Geophysical Research Letters, 31, 2004.

697   Miller, R., Tegen, I., and Perlwitz, J.: Surface radiative forcing by soil dust aerosols and the hydrologic

698   cycle, Journal of Geophysical Research: Atmospheres, 109, 2004.

699   Mlawer, E. J., Taubman, S. J., Brown, P. D., Iacono, M. J., and Clough, S. A.: Radiative transfer for

700   inhomogeneous atmospheres: RRTM, a validated correlated-k model for the longwave, Journal of

701   Geophysical Research: Atmospheres, 102, 16663-16682, 1997.

702   Nabat, P., Somot, S., Mallet, M., Michou, M., Sevault, F., Driouech, F., Meloni, D., Di Sarra, A., Di Biagio,

703   C., and Formenti, P.: Dust aerosol radiative effects during summer 2012 simulated with a coupled regional

704   aerosol–atmosphere–ocean model over the Mediterranean, Atmospheric Chemistry and Physics, 15, 3303-

705   3326, 2015a.

706   Nabat, P., Somot, S., Mallet, M., Sevault, F., Chiacchio, M., and Wild, M.: Direct and semi-direct aerosol

707   radiative effect on the Mediterranean climate variability using a coupled regional climate system model,

708   Climate dynamics, 44, 1127-1155, 2015b.

709   Perlwitz, J., and Miller, R. L.: Cloud cover increase with increasing aerosol absorptivity: A counterexample

710   to the conventional semidirect aerosol effect, Journal of Geophysical Research: Atmospheres, 115, 2010.

711   Phillips, V. T., DeMott, P. J., and Andronache, C.: An empirical parameterization of heterogeneous ice

712   nucleation for multiple chemical species of aerosol, Journal of the atmospheric sciences, 65, 2757-2783,

713   2008.

714   Seigel, R., Van Den Heever, S., and Saleeby, S.: Mineral dust indirect effects and cloud radiative feedbacks

715   of a simulated idealized nocturnal squall line, Atmospheric Chemistry and Physics, 13, 4467-4485, 2013.

716   Shao: A model for mineral dust emission, Journal of Geophysical Research: Atmospheres, 106, 20239-

717   20254, 2001.

718   Shao: Simplification of a dust emission scheme and comparison with data, Journal of Geophysical Research:

719   Atmospheres, 109, 2004.

720   Shao, Ishizuka, M., Mikami, M., and Leys, J.: Parameterization of size-resolved dust emission and

721   validation with measurements, Journal of Geophysical Research: Atmospheres, 116, 2011.

722   Soil Survey Staff: Soil survey manual, 1993.

723 Solomos, S., Kallos, G., Kushta, J., Astitha, M., Tremback, C., Nenes, A., and Levin, Z.: An integrated

724 modeling study on the effects of mineral dust and sea salt particles on clouds and precipitation, Atmospheric

725 Chemistry and Physics, 11, 873-892, 2011.

726 Su, L., and Fung, J. C.: Sensitivities of WRF-Chem to dust emission schemes and land surface properties

727 in simulating dust cycles during springtime over East Asia, Journal of Geophysical Research: Atmospheres,

728 120, 2015.

729 Tesfaye, M., Tsidu, G. M., Botai, J., and Sivakumar, V.: Mineral dust aerosol distributions, its direct and

730 semi-direct effects over South Africa based on regional climate model simulation, Journal of Arid

731 Environments, 114, 22-40, 2015.

732 Textor, C., Schulz, M., Guibert, S., Kinne, S., Balkanski, Y., Bauer, S., Berntsen, T., Berglen, T., Boucher,

733 O., and Chin, M.: Analysis and quantification of the diversities of aerosol life cycles within AeroCom,

734 Atmospheric Chemistry and Physics, 6, 1777-1813, 2006.

735 Thompson, G., Rasmussen, R. M., and Manning, K.: Explicit forecasts of winter precipitation using an

736 improved bulk microphysics scheme. Part I: Description and sensitivity analysis, Monthly Weather Review,

737 132, 519-542, 2004.

738 Thompson, G., and Eidhammer, T.: A study of aerosol impacts on clouds and precipitation development in

739 a large winter cyclone, Journal of the Atmospheric Sciences, 71, 3636-3658, 2014.

740 Tomasi, C., Fuzzi, S., and Kokhanovsky, A.: Atmospheric Aerosols: Life Cycles and Effects on Air Quality

741 and Climate, John Wiley & Sons, 2017.

742 Twohy, C. H., Kreidenweis, S. M., Eidhammer, T., Browell, E. V., Heymsfield, A. J., Bansemer, A. R.,

743 Anderson, B. E., Chen, G., Ismail, S., and DeMott, P. J.: Saharan dust particles nucleate droplets in eastern

744 Atlantic clouds, Geophysical Research Letters, 36, 2009.

745 Vaughan, M. A., Young, S. A., Winker, D. M., Powell, K. A., Omar, A. H., Liu, Z., Hu, Y., and Hostetler,

746 C. A.: Fully automated analysis of space-based lidar data: An overview of the CALIPSO retrieval

747 algorithms and data products, Remote Sensing, 2004, 16-30.

748 Wesely, M.: Parameterization of surface resistances to gaseous dry deposition in regional-scale numerical

749 models, Atmospheric Environment (1967), 23, 1293-1304, 1989.

750 Winker, Pelon, J., Coakley Jr, J., Ackerman, S., Charlson, R., Colarco, P., Flamant, P., Fu, Q., Hoff, R.,

751 and Kittaka, C.: The CALIPSO mission: A global 3D view of aerosols and clouds, Bulletin of the American

752 Meteorological Society, 91, 1211-1229, 2010.

753 Winker, D. M., Vaughan, M. A., Omar, A., Hu, Y., Powell, K. A., Liu, Z., Hunt, W. H., and Young, S. A.:

754 Overview of the CALIPSO mission and CALIOP data processing algorithms, Journal of Atmospheric and

755 Oceanic Technology, 26, 2310-2323, 2009.

756 Zhang, C., Wang, M., Morrison, H., Somerville, R. C., Zhang, K., Liu, X., and Li, J. L. F.: Investigating

757 ice nucleation in cirrus clouds with an aerosol-enabled Multiscale Modeling Framework, Journal of

758 Advances in Modeling Earth Systems, 6, 998-1015, 2014.

759

760

31

786   Figure 11: Vertical profiles for the mean observed IWC from CALIPSO, and the simulated IWC with various c_f for

787   the dust events on March 21, April 1, April 9, and April 23, 2012.

788   Figure 12: Vertical profiles for the mean observational IWC from CALIPSO, and the simulated IWC with threshold

789   RH values of 105% and 100% for the dust events on March 21, April 1, April 9, and April 23, 2012.

Table 1: Performance statistics for the model in simulating surface PM_{10} concentrations at environmental monitoring stations during the simulation period.

City	STATION NO.	MB (μg/m3)	ME (μg/m3)	RMSE (μg/m3)	r
BAOTOU	XCNAQ77	-36.18	80.43	94.88	0.59
	XCNAQ79	-10.05	75.83	106.58	0.62
SHIZUISHAN	XCNAQ346	72.46	121.18	317.73	0.79
	XCNAQ347	17.64	147.95	294.71	0.75
JINCHANG	XCNAQ340	-108.73	109.09	128.56	0.77
	XCNAQ342	-18.65	46.07	64.78	0.70
YAN'AN	XCNAQ335	-38.93	99.05	149.44	0.68
	XCNAQ336	-60.15	124.74	166.89	0.60
YINCHUAN	XCNAQ344	33.97	112.26	240.27	0.87
	CN_1487	-39.62	155.83	249.00	0.62
Average		-18.84	107.24	181.28	0.70

MB: mean bias; ME: mean error; RMSE: root mean squared error; r: correlation coefficient.
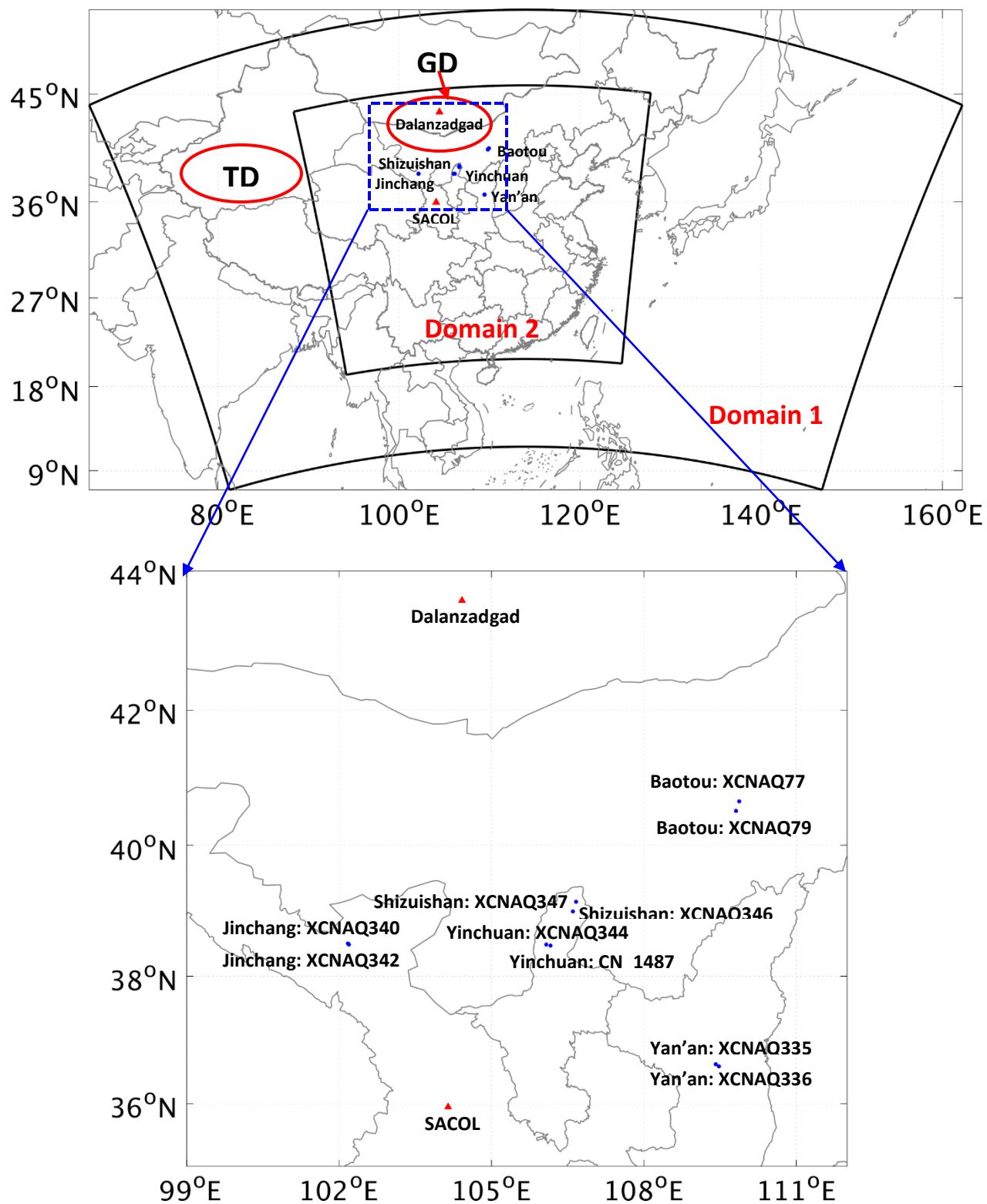
Figure 1: Nested domain set for the simulations. Blue dots represent the ten monitoring stations used for model validation. TD: the Taklimakan Desert; GD: The Gobi Desert.
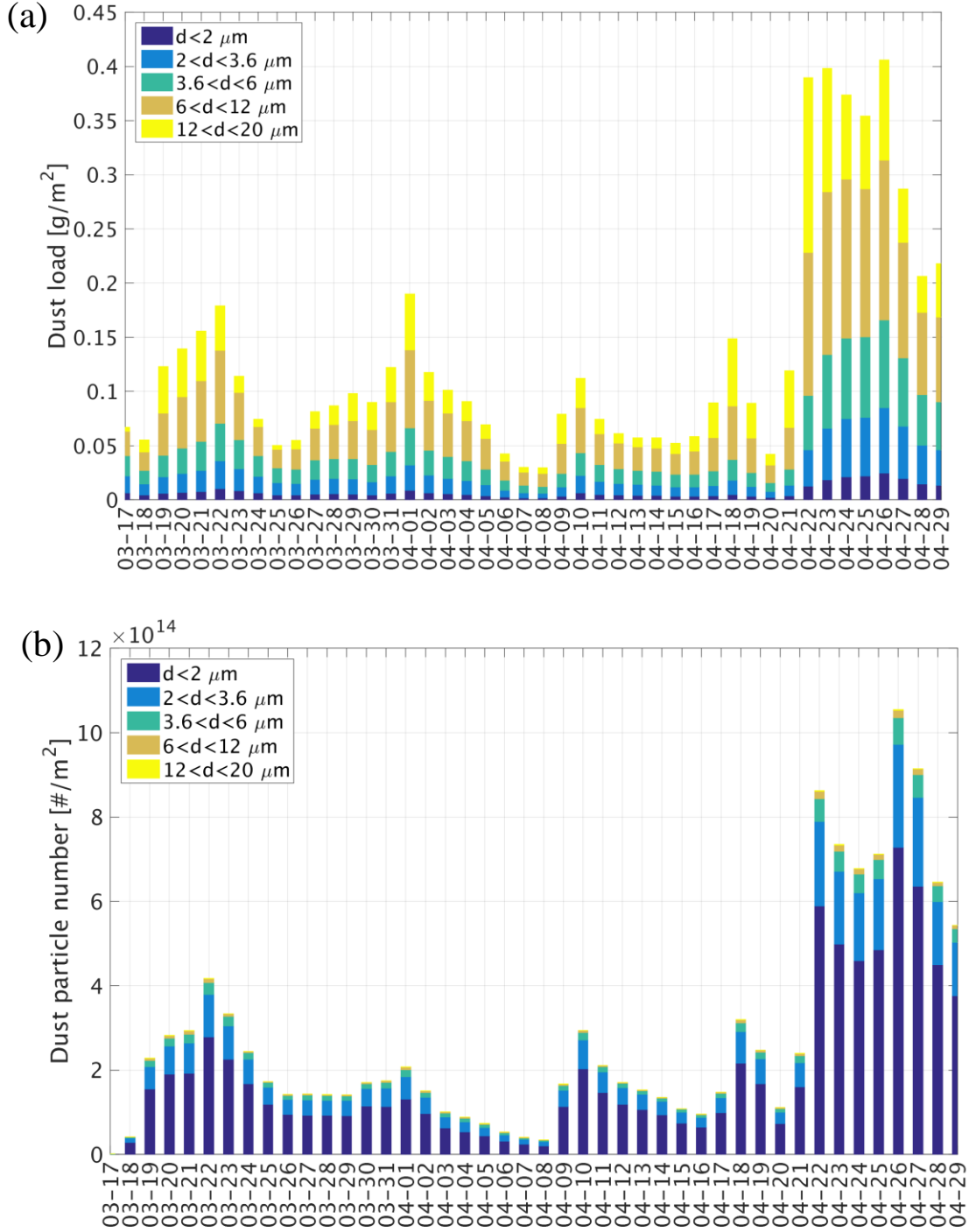
Figure 2: Time series of spatially averaged daily dust mass load (a) and daily number density of dust particles (b) over East Asia (domain 1) during the simulation period.
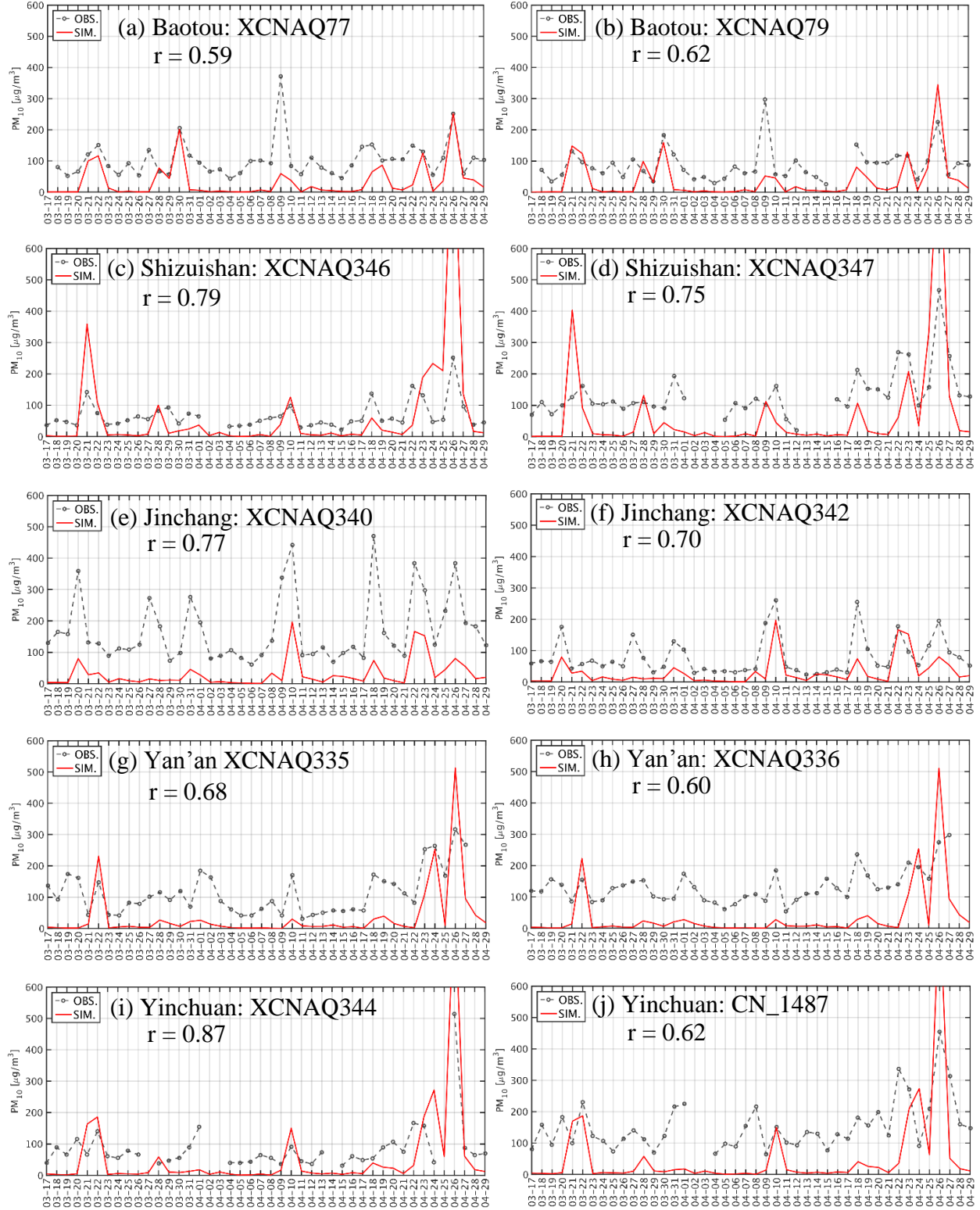
Figure 3: Time series of hourly observed and simulated surface PM_{10} concentrations at various environmental monitoring stations. r represents the correlation coefficient between simulation results and observations.
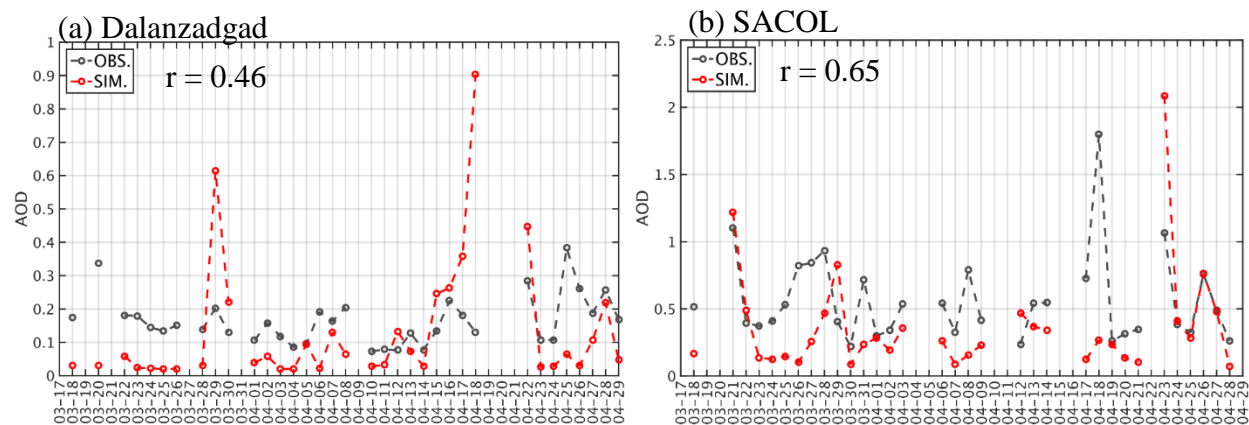
Figure 4: Time series of daily mean observed and simulated aerosol optical depths at Dalanzadgad (a) and SACOL (b). r represents the correlation coefficient between simulation results and observations.
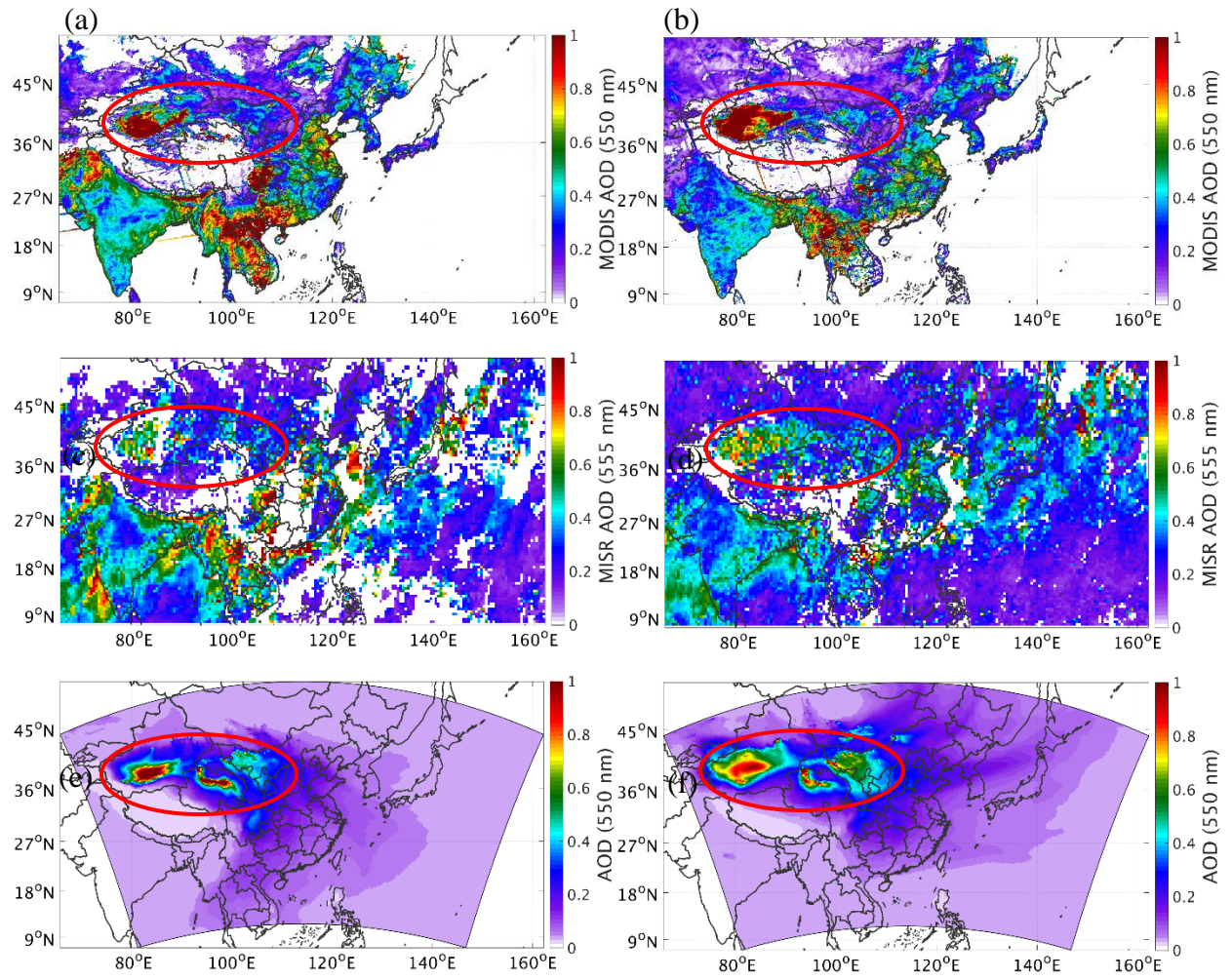
Figure 5: Spatial distributions of monthly mean AOD from MODIS observations (a, b), MISR observations (c, d), and simulation results (e, f) for March (left panel) and April (right panel) of 2012.
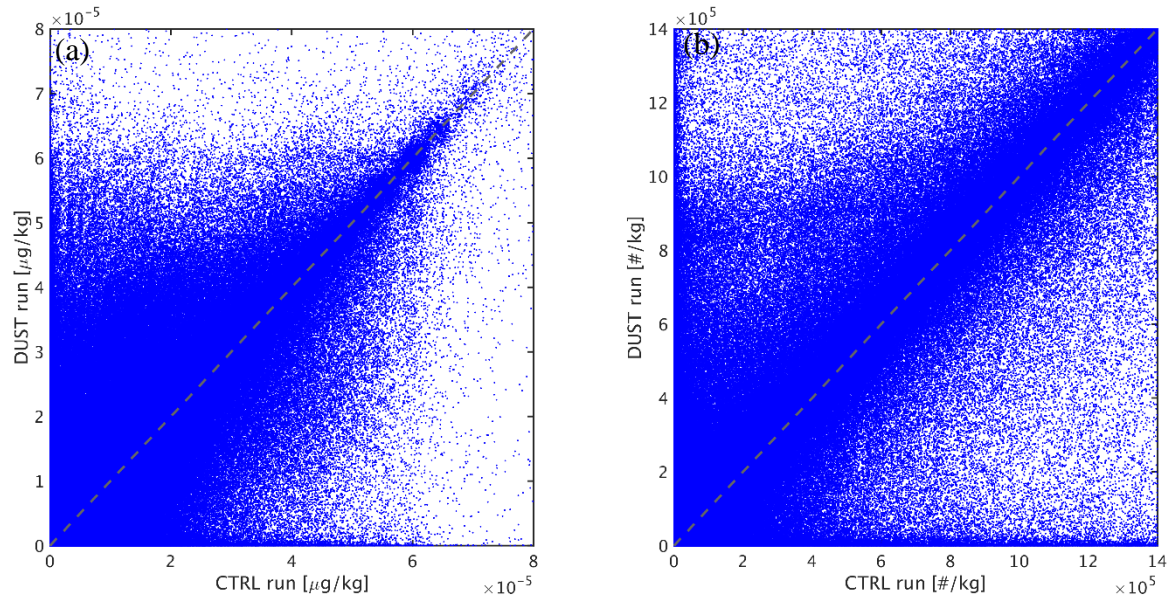
Figure 6: Simulated cloud ice mixing ratio (a) and cloud ice crystal number concentration (b) at each data point from CTRL and DUST.
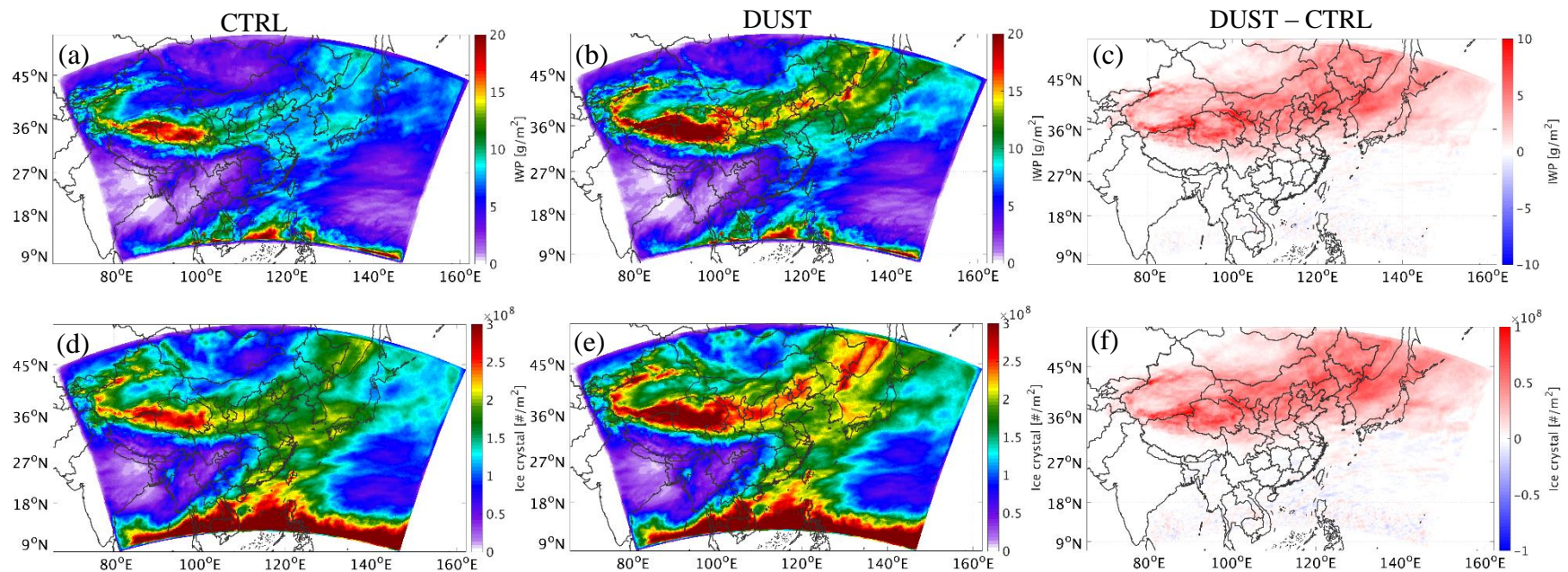
Figure 7: Spatial distributions for the temporal mean simulated cloud ice water path (a-c) and ice crystal number density (d-f) from CTRL (left panel), DUST (middle panel), and the difference between CTRL and DUST (right panel) over East Asia (domain 1) during the simulation period.
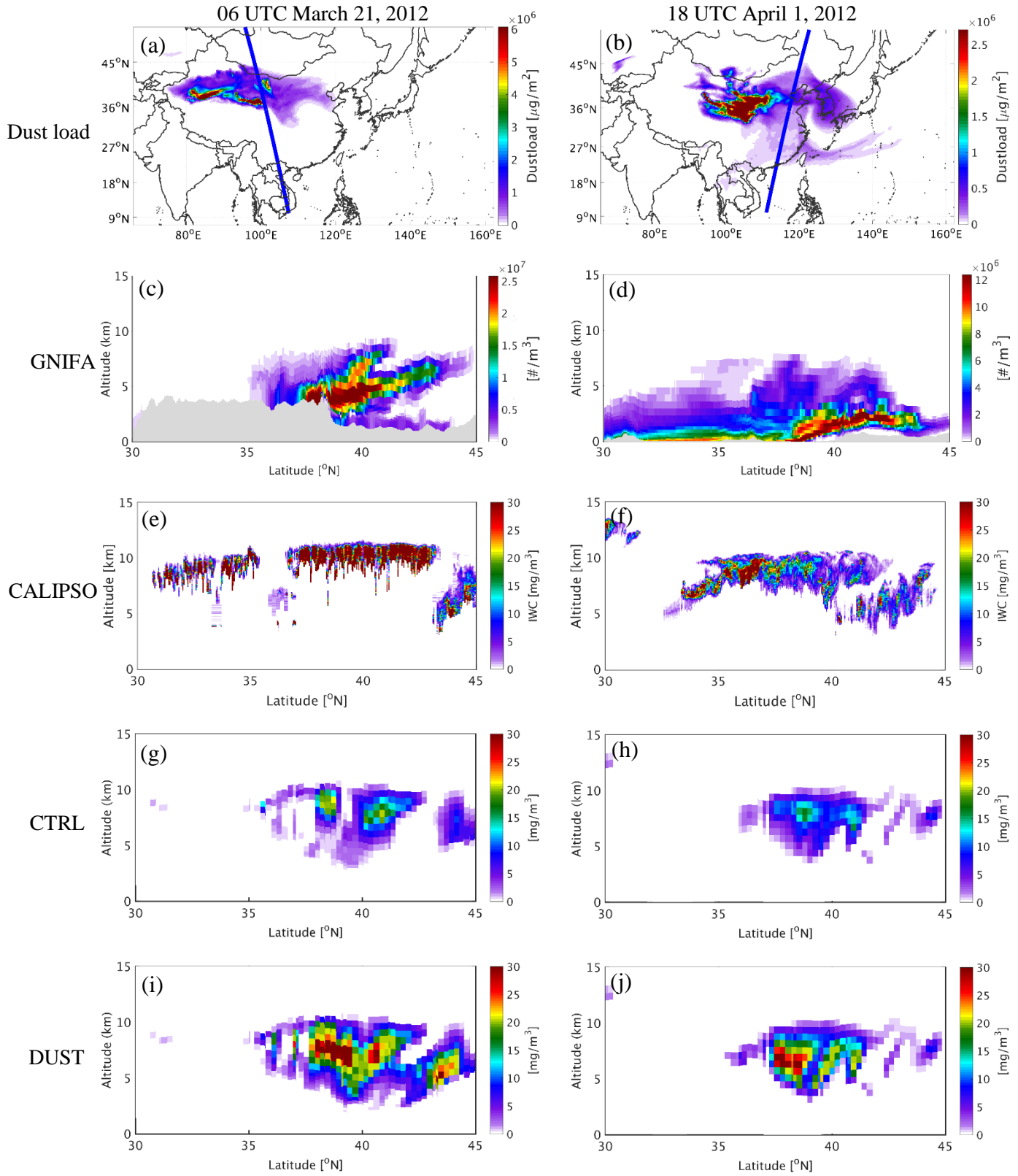
Figure 8: Spatial distribution for simulated dust load and satellite scanning track (a, b); the simulated vertical profile of ice-friendly aerosol (GNIFA) number concentration (c, d), with the orography represented by the shaded area; the CALIPSO vertical profile of IWC (e, f); and the simulated vertical profile of IWC from CTRL (g, h) and DUST (i, j) for the case on March 21 (left panel) and April 1 (right panel) of 2012.
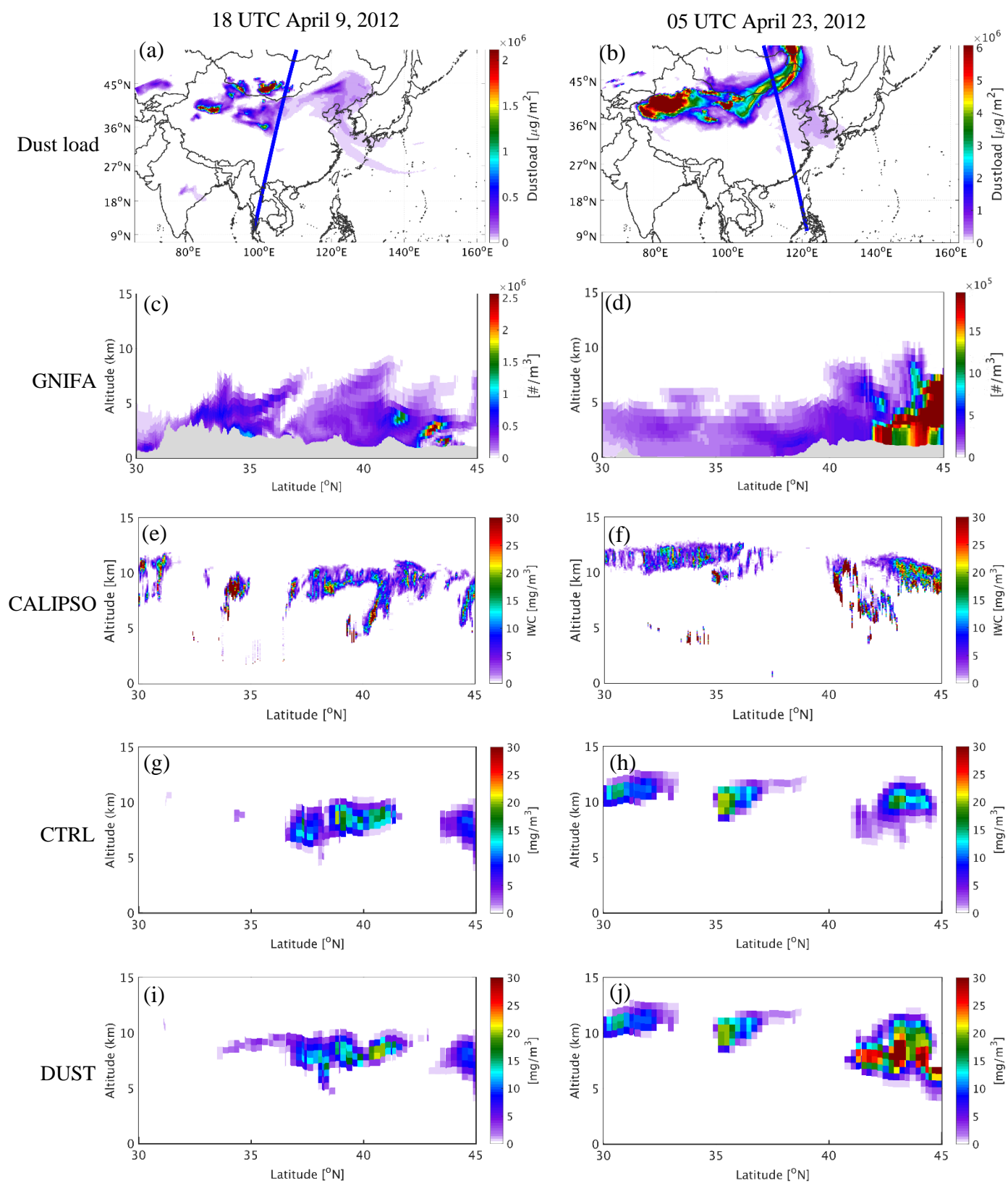
41

Figure 9: As Figure 8 but for the cases on April 9 (left panel) and April 23, (right panel) of 2012.
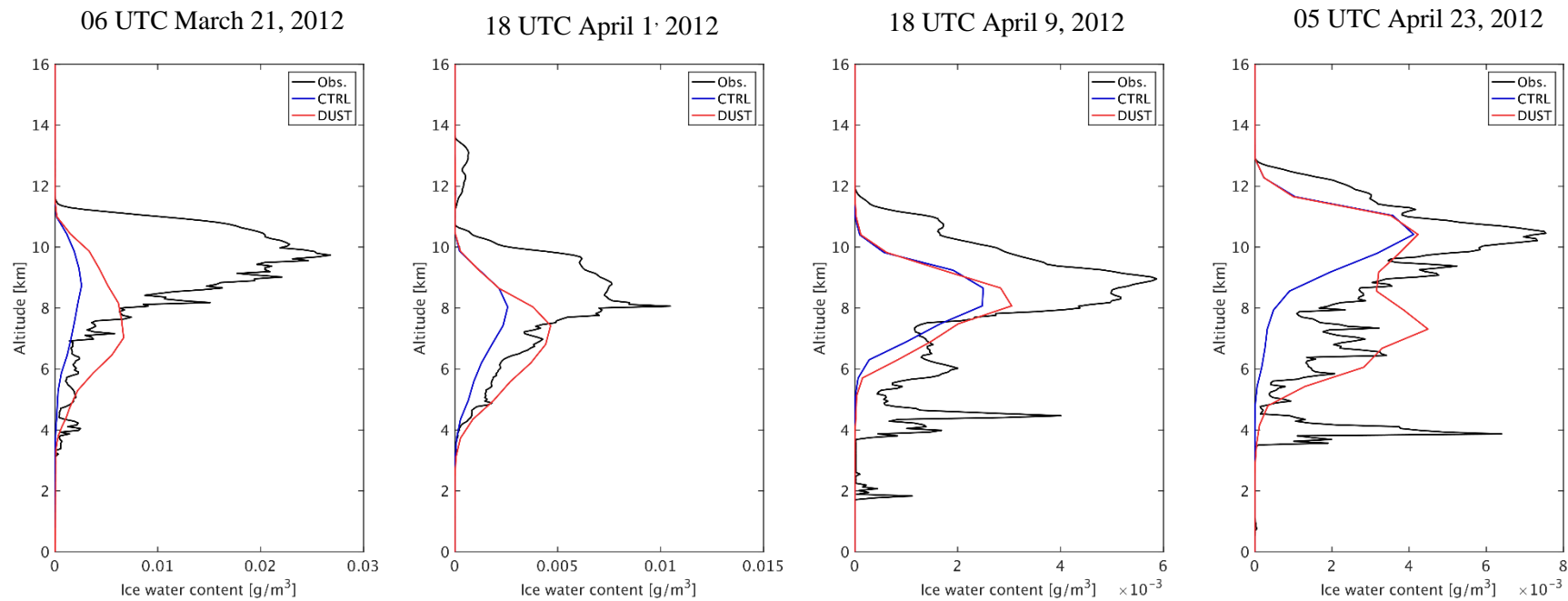
Figure 10: Vertical profiles for the mean observed IWC from CALIPSO, and the simulated IWC from CTRL and DUST for dust events on March 21, April 1, April 9, and April 23, 2012.
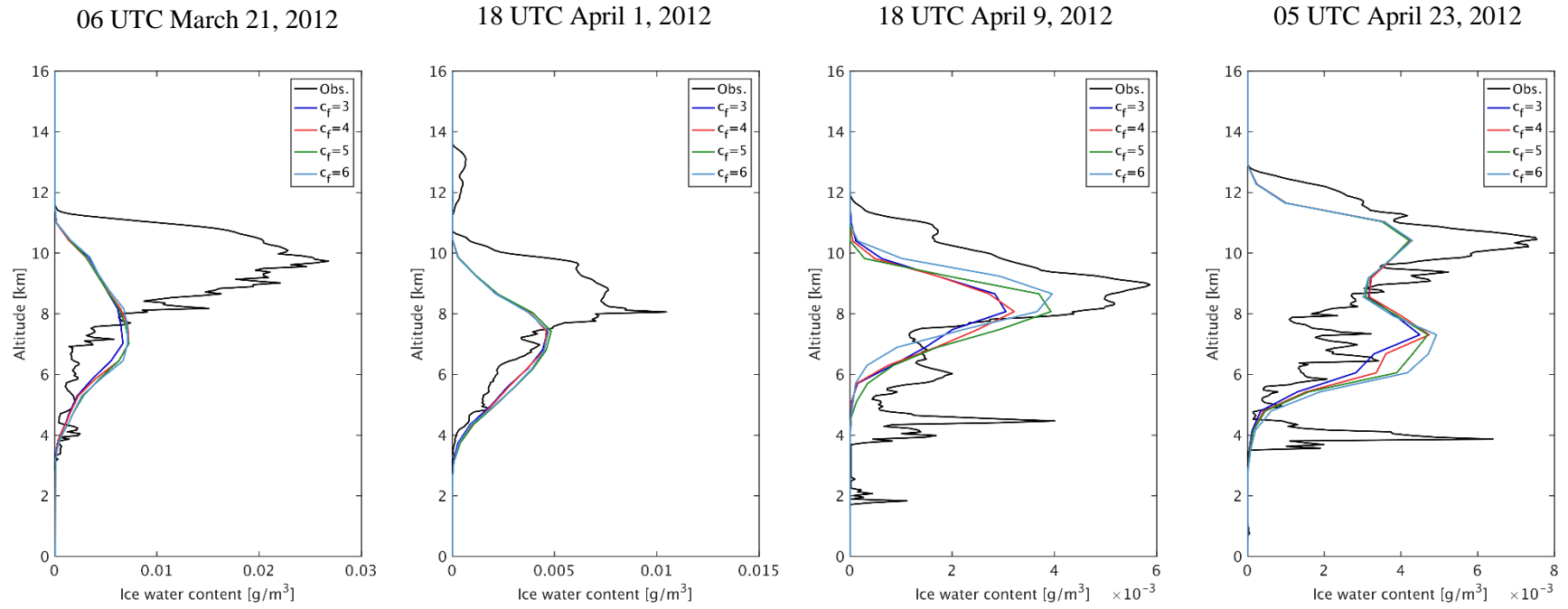
Figure 11: Vertical profiles for the mean observed IWC from CALIPSO, and the simulated IWC with various c_f for the dust events on March 21, April 1, April 9, and April 23, 2012.
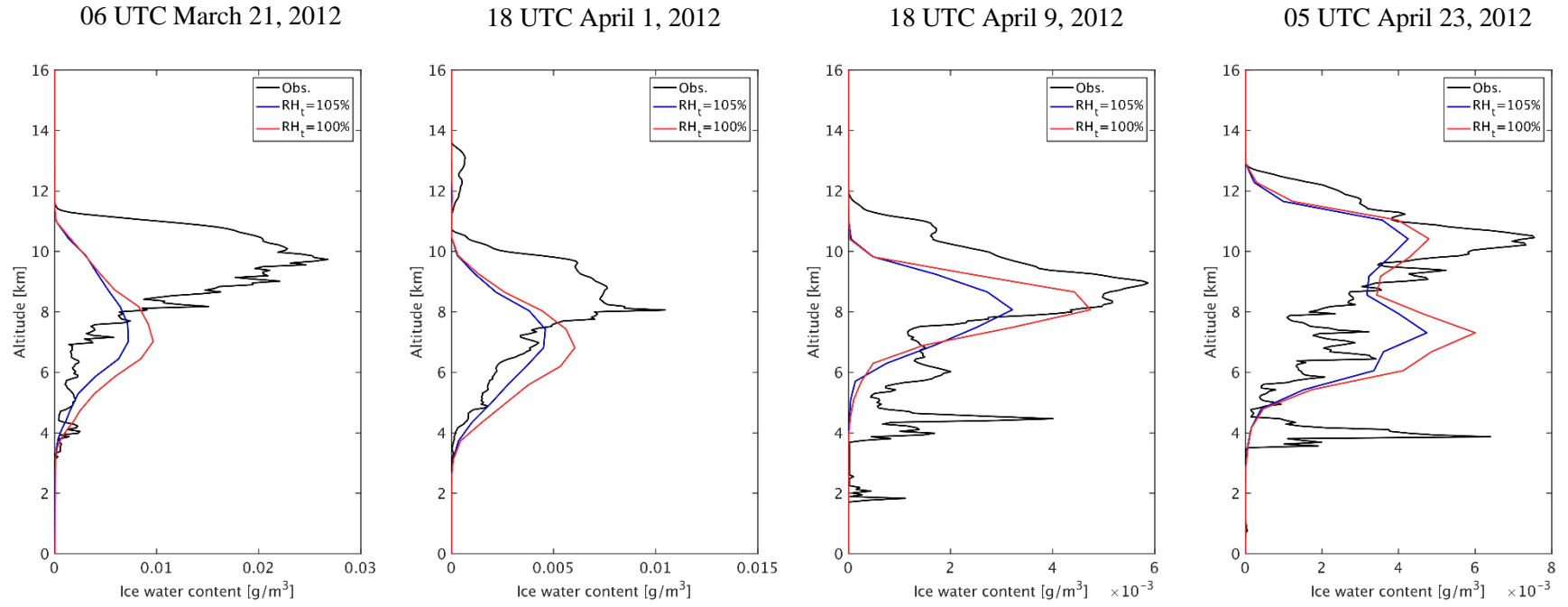
Figure 12: Vertical profiles for the mean observational IWC from CALIPSO, and the simulated IWC with threshold RH values of 105% and 100% for the dust events on March 21, April 1, April 9, and April 23, 2012.